

Simulations of a late lunar-forming impact

Robin M. Canup

Southwest Research Institute, Department of Space Studies, 1050 Walnut St. Suite 400, Boulder, CO 80302, USA

Received 16 June 2003; revised 15 September 2003

Abstract

Results of about 100 hydrodynamic simulations of potential Moon-forming impacts are presented, focusing on the “late impact” scenario in which the lunar forming impact occurs near the very end of Earth’s accretion (Canup and Asphaug, 2001, *Nature* 412, 708–712). A new equation of state is utilized that includes a treatment of molecular vapor (“M-ANEOS”; Melosh, 2000, in: *Proc. Lunar Planet. Sci. Conf.* 31st, p. 1903). The sensitivity of impact outcome to collision conditions is assessed, in particular how the mass, angular momentum, composition and origin (target vs. impactor) of the material placed into circumterrestrial orbit vary with impact angle, speed, impactor-to-target mass ratio, and initial thermal state of the colliding objects. The most favorable conditions for producing a sufficiently massive and iron-depleted protolunar disk involve collisions with an impact angle near 45 degrees and an impactor velocity at infinity < 4 km/sec. For a total mass and angular momentum near to that of the current Earth–Moon system, such impacts typically place about a lunar mass of material into orbits exterior to the Roche limit, with the orbiting material composed of 10 to 30% vapor by mass. In all cases, the vast majority of the orbiting material originates from the impactor, consistent with previous findings. By mapping the end fate (escaping, orbiting, or in the planet) of each particle and the peak temperature it experiences during the impact onto the figure of the initial objects, it is shown that in the successful collisions, the impactor material that ends up in orbit is primarily that portion of the object that was heated the least, having avoided direct collision with the Earth. Using these and previous results as a guide, a continuous suite of impact conditions intermediate to the “late impact” (Canup and Asphaug, 2001, *Nature* 412, 708–712) and “early Earth” (Cameron, 2000, in: Canup, R.M., Righter, K. (Eds.), *Origin of the Earth and Moon*, pp. 133–144; 2001, *Meteorit. Planet. Sci.* 36, 9–22) scenarios is identified that should also produce iron-poor, \sim lunar-sized satellites and a system angular momentum similar to that of the Earth–Moon system. Among these, those that leave the Earth $> 95\%$ accreted after the Moon-forming impact are favored here, implying a giant impactor mass between 0.11 and 0.14 Earth masses.

© 2003 Elsevier Inc. All rights reserved.

Keywords: Moon; Impact processes; Planetary formation; Satellites, formation

1. Background

The origin of the Moon is one of the oldest and most studied problems in planetary science. The Moon’s lack of a large iron core—together with planet accretion model predictions that large impacts would be common—led Hartmann and Davis (1975) to postulate that an impact with the Earth could have ejected iron-depleted mantle material into orbit from which the Moon then formed. They also suggested that ejected material might be depleted in volatile elements relative to the Earth. An independent and contemporaneous investigation by Cameron and Ward (1976) recognized that the oblique impact of a roughly Mars-sized

planet could account for the rapid initial terrestrial rotation rate implied by the current angular momentum of the Earth–Moon system, and suggested that vaporization might provide a physical mechanism to emplace material into bound orbit. The concepts described in these two works contain the basic elements of what is now the leading theory for lunar origin, the giant impact hypothesis.

Several decades of works have utilized increasingly sophisticated numerical simulations—primarily smooth particle hydrodynamics (or SPH)—to model the hypothesized impact event. Early works were challenged by slow computational times dictating necessarily low numerical resolutions (Benz et al., 1986, 1987, 1989; Cameron and Benz, 1991); in these, a collision was represented by 3000 SPH particles, so that a lunar mass of ejected material was de-

E-mail address: robin@boulder.swri.edu.

scribed by just 37 particles. Order-of-magnitude improvements in resolution are now possible (Cameron, 2000, 2001; Canup and Asphaug, 2001), and 10^4 – 10^5 particle simulations allow for a more detailed description of the ejected material.

Despite these computational advances, identifying impacts capable of placing sufficient mass into Earth orbit to yield the Moon while also accounting for the Earth–Moon system mass and angular momentum proved challenging. Since Cameron and Benz (1991), progressively larger impactors relative to the targets were considered in an effort to increase the yield of orbiting material, with Cameron (2000, 2001) considering collisions that all involved impactors containing 30% of the total colliding mass. The type of impact favored by those works involved an impactor with roughly twice the mass of Mars and an impact angular momentum close to that of the current Earth–Moon system, L_{EM} , but with a total mass (impactor plus target) of only $M_T \sim 0.65M_{\oplus}$. In this so-called “early-Earth” scenario, the Earth is only partially accreted when the Moon forms and must subsequently gain $\sim 0.35M_{\oplus}$, with the later growth involving sufficiently small and numerous impacts so that the system angular momentum is not drastically altered. It is not clear that such a large quantity of small material would exist at this late stage of planet accretion; e.g., Weidenschilling et al. (1997) find only about 10% of the mass in the terrestrial region is contained in objects smaller than lunar size after 1 million years, and dating of the lunar forming impact inferred from the Hf–W system places it much later at ~ 30 million years (e.g., Halliday et al., 2000; Yin et al., 2002; Jacobsen and Yin, 2003). Another difficulty is the potential for the Moon to become contaminated by iron-rich material during the post-impact interval when the Earth had to accumulate the final $\sim 35\%$ of its mass (e.g., Stewart, 2000). If the Moon accreted a proportionate share based on its physical cross-section, the Earth could only accrete $\sim 0.06M_{\oplus}$ of terrestrial composition material before the Moon gained more than 10% of its mass in iron. There are factors that could mitigate this, including a less than perfect lunar accretion efficiency (e.g., Morishima and Watanabe, 2001). However in general, as the amount of material which must be added to the Earth after the Moon-forming impact in a given impact scenario increases, difficulties with the Moon becoming compositionally more similar to the Earth and the other terrestrial planets also increase.

Work has been ongoing to identify other impact scenarios that can more closely produce the Earth–Moon system. Canup et al. (2001) re-examined results of Cameron (2000), and identified trends consistent across all of the simulations when results were viewed in terms of scaled quantities. In particular, it was shown that for the impactor-to-total mass ratio of $\gamma = 0.3$ utilized by Cameron (2000, 2001), the maximum yield of orbiting material resulted for an impact angular momentum about 70 to 80% of that of a

grazing impact, L_{graz} , independent of the total colliding mass, M_T .

Utilizing the scaling analysis in Canup et al. (2001), Canup and Asphaug (2001, hereafter CA01) predicted that the maximum yield for an $L \approx L_{EM}$ and $M_T \approx M_{\oplus}$ impact should be achieved when $L_{EM}/L_{graz} \approx 0.8$; this gave a predicted optimal impactor-to-total mass ratio of $\gamma \sim 0.1$, or an approximately Mars-sized object.¹ In a survey of 36 simulations, they found a variety of successful candidate impacts that produced massive and iron-depleted disks, together with a final system with $M_T \approx M_{\oplus}$ and $L \approx L_{EM}$. For this “late impact” case, the Moon forming event occurs at the very end of Earth’s accretion; this scenario is attractive in that it requires little or no subsequent dynamical modification of the Earth–Moon system.

However, in their simulations CA01 utilized a simple equation of state, Tillotson (1962), which lacks a consistent thermodynamical treatment of vaporization and mixed phase states. This is a key weakness for modeling lunar-forming impacts because of the potentially important role of pressure gradients in placing material into orbit (e.g., Cameron and Ward, 1976; Stevenson, 1987; Melosh and Kipp, 1989). A sophisticated, semi-analytic equation of state known as ANEOS (Thompson and Lauson, 1972) has been utilized by previous giant impact studies (Benz et al., 1989; Cameron and Benz, 1991; Cameron, 1997, 2000, 2001). Unlike Tillotson, ANEOS handles phase changes and mixed phases in a thermodynamically consistent manner; however, in its standard rendition ANEOS treats all vapor as monatomic species (e.g., Melosh and Pierazzo, 1997). The entropy and energy required for vaporization of molecular species—such as mantle rock—is therefore overestimated, which may be responsible for the apparent lack of vapor production in recent high-resolution simulations (Cameron, 2000, 2001).²

Recently, an extension to ANEOS to allow for molecular vapor has been undertaken by Melosh (2000). In this work, we utilize Melosh’s new ANEOS (which we refer to hereafter as M-ANEOS) in ~ 100 SPH simulations that each involve between $N = 20,000$ and $120,000$ particles; the latter are the highest resolution giant impact simulations published to date. We focus on the “late impact” scenario of CA01, considering a range of impactor sizes, impact angles, initial thermal states and impact velocities. Our overall objective is to determine the types of impacts capable of producing the Earth–Moon system, and the dynamical, compositional and thermal implications for the post-impact Earth and protolunar disk.

¹ Impactors with $\gamma < 0.12$ had been ruled out as lunar forming candidates in early low-resolution studies using the Tillotson equation of state (Benz et al., 1987), because they appeared to produce overly iron-rich disks. However those simulations were unable to adequately resolve the disk iron, and were extremely limited in number due to their computational demands at that time.

² In addition, there have been problems with the use of this equation of state in recent simulations (Cameron, 2000), as temperatures in the Earth’s interior decrease to 0 K.

2. Key constraints

The lunar forming impact is constrained by basic properties of the Earth–Moon system:

- (i) the system angular momentum, $L_{EM} \equiv 3.5 \times 10^{41}$ g-cm²/sec,
- (ii) the masses of the Earth and Moon ($M_L = 7.35 \times 10^{25}$ g = $0.0123M_{\oplus}$), and
- (iii) the observed degree of lunar iron depletion.

The angular momentum of the Earth–Moon system has likely decreased somewhat subsequent to lunar formation due to solar interactions, and/or the accretion of additional small material onto the Earth–Moon system after the Moon-forming impact. Direct solar tides on the Earth could remove $O(10^{-2})L_{EM}$ (e.g., Canup et al., 2001); interaction of the Moon with the so-called evection resonance—where the lunar apsidal precession period equals one year—(Kaula and Yoder, 1976; Touma and Wisdom, 1998) could significantly increase its orbital eccentricity and thus act to reduce the system angular momentum (Kaula and Yoder, 1976). The co-accretion of even $\sim 10\%$ of an Earth mass in small material after the Moon forming impact could produce $\Delta L/L_{EM} \sim O(10^{-1})$ through the loss of lunar impact ejecta (Morishima and Watanabe, 2001). Given this, we consider viable impacts to be those that leave an Earth-disk system with $1.0 \leq L \leq 1.2L_{EM}$.

A lunar mass satellite on a circular orbit with $a = a_R$ (where $a_R \equiv 2.456R_p(\rho_p/\rho)^{1/3} \approx 2.9R_{\oplus}$ is the Earth's Roche limit for lunar density materials), would contain an orbital angular momentum of $M_L\sqrt{GM_{\oplus}a_{Roche}} \approx 0.18L_{EM}$, providing a lower limit on the mass and angular momentum of orbiting material necessary to yield the Moon assuming completely efficient accumulation. In reality, much of the orbiting material initially within a_R will re-impact the Earth in the course of angular momentum exchange within the protolunar disk and through interaction with the forming Moon (e.g., Ida et al., 1997; Canup and Ward, 2000); some may also be ejected from the system entirely.

Simulations of accretion in a protolunar disk (Ida et al., 1997; Kokubo et al., 2000; review by Kokubo et al., 2000) predict the formation of a satellite with a characteristic orbital radius $\sim 1.2a_R$, or $a \sim 3.5R_{\oplus}$. A basic conservation argument can be made to estimate the mass of a satellite, M_M , forming with $a = 1.2a_R$ from an initial disk containing mass M_D and angular momentum L_D (Ida et al., 1997):

$$M_M \equiv 1.9L_D/\sqrt{GM_{\oplus}a_R} - 1.1M_D - 1.9M_{esc}, \quad (1)$$

where M_{esc} is the mass that escapes during disk evolution. Equation (1) assumes that all of the mass and angular momentum in the disk will eventually either become incorporated into a single satellite, be lost to the protoearth as the disk viscously spreads, or escape. Such a relationship should be approximately valid over a wide range of potential disk

evolution and satellite accretion time scales, so long as the final state is a moon formed near the Roche limit and there is no additional post-impact source of angular momentum or mass to the disk. The latter condition could be violated if, e.g., tidal interactions of disk material with the Earth led to a positive torque on the disk on a time scale less than or comparable to the accretion time. This may be possible if there are coherent structures in the disk such as spiral waves (Ward, 1998), and would lead to a higher value for M_M than that implied by Eq. (1). Here we use Eq. (1) to estimate the mass of the satellite that will result from the orbiting disks produced in our simulations assuming³ $(M_{esc}/M_D) = 0.05$.

There are two reservoirs for iron in the Moon: a potential lunar core containing metallic Fe, and the silicate lunar mantle/crust, containing FeO. Indirect seismic and gravitational analyses suggest the presence of a small lunar core, containing 0.01 to $0.03M_L$ (e.g., Hood and Zuber, 2000); a similarly sized core is also consistent with that needed to account for the lunar siderophile depletion pattern (e.g., Jones and Palme, 2000; Righter, 2002). By comparison, the Earth's core contains about $0.32M_{\oplus}$, with approximately $0.27M_{\oplus}$ in iron, while the terrestrial mantle contains about 6% iron by mass in the form of FeO, for a total terrestrial iron abundance of about 31% (e.g., Jones and Palme, 2000). The Moon is believed to be enriched in FeO relative to the Earth's mantle; an iron mass fraction ~ 7 to 8% has been measured for lower lunar crustal material (e.g., Lucey et al., 1995), and lunar composition models predict 8 to 10% Fe in FeO (e.g., Jones and Delano, 1989; also Jones and Palme, 2000). Using a simpler approach based on the lunar bulk density $\rho_L = 3.34$ g/cm³, and the assumption that all lunar iron is oxidized and contained in low density silicates, Wood (1986) estimated that the Moon contains no more than $\sim 8\%$ iron by mass. Thus although there are considerable uncertainties, the overall lunar mass fraction of elemental iron is likely in the few to 10% range.

Compared to these distinctions, the treatment of Fe in our simulations is very simplistic. We assume our impactors and targets are composed of 30% iron by mass, contained entirely in their cores, and consider as viable lunar-forming candidates those impacts that produce a sufficiently massive orbiting disk with $< 10\%$ iron by mass overall, and $< 5\%$ iron in the material with equivalent orbits exterior to the Roche limit.

3. Approach

The method utilized here is smooth particle hydrodynamics, or SPH (e.g., Lucy, 1977). Our specific code (see Appendix A) is a descendant of that of Benz et al. (1989),

³ The $(M_{esc}/M_D) = 0.05$ value was obtained by accretion simulations of more centrally condensed disks than those typically found here (e.g., Ida et al., 1997); the fractional disk mass escaping during accretion could be higher than this for initially more radially extended disks.

a cousin to that utilized in recent works by Cameron (e.g., Cameron, 1997, 2000, 2001), and identical to that used in CA01, save the switch to a new equation of state as described below.

SPH is a Lagrangian technique in which the modeled material is represented by a great number of spherically symmetric overlapping ‘particles’ whose individual evolutions are tracked as a function of time. Each particle represents a quantity of mass of a given composition, whose 3-dimensional spatial extent is specified by a density weighting function known as the kernel, and the characteristic spatial width of the particle, known as the smoothing length, h . The functional form of the kernel does not change during a simulation, but the smoothing length of each particle is adjusted so as to maintain an overlap with a desired number of other particles, thus allowing even low-density regions to be smoothly resolved.⁴ SPH is well suited to intensely deforming systems evolving within mostly empty space, since the code resolution follows the material evolution. It also allows for easy tracking of material and compositional identities/histories.

The evolution of each particle’s kinematic (position and velocity) and state (internal energy, density) variables are evolved due to (1) gravity, (2) compressional heating and expansional cooling, and (3) shock dissipation.⁵ The chosen form for the equation of state relates a particle’s specific internal energy and local density to pressure at each time step. The time step is Courant limited; for the run times considered here, the typical energy error is $\Delta E/E \sim 10^{-3}$, and angular momentum is conserved to 1 part in 10^4 over the entire computational volume.

3.1. ANEOS with molecular vapor

We use the equation of state (EOS) known as ANEOS (Thompson and Lauson, 1972; see also Benz et al., 1989; Melosh, 2000). In ANEOS, thermodynamic quantities in all states are derived from the Helmholtz free energy, F , with temperature, T , and density, ρ , as independent variables. ANEOS describes F as a sum of three components: a zero-temperature free energy, a nuclear component, and an electronic term that accounts for ionization. The nuclear component is determined via an interpolation function that at low temperatures approximates a crystalline Debye solid and at high temperatures, an ideal gas. ANEOS describes mixed phase states (e.g., a two-phase vapor and melt) by treating the different phases as separate components that are in tem-

perature and pressure equilibrium.⁶ Thus a two-phase state within a single SPH particle is treated in a thermodynamically self-consistent manner, and the mass fraction contained in each phase is computed.

ANEOS has been utilized in previous giant impact simulations (e.g., Benz et al., 1989; Cameron and Benz, 1991; Cameron, 1997, 2000, 2001). However, the standard ANEOS treats all vapor as non-interacting monatomic species. This approximation was developed for metals, but overestimates the energy and entropy required for vaporization for molecular materials, such as a mantle silicate (Melosh and Pierazzo, 1997; Melosh, 2000). Melosh (2000) has recently revised ANEOS to include treatment of a vapor containing bound diatomic molecules (e.g., SiO or MgO for forsterite, Mg_2SiO_4), by adding a term to F that vanishes as the predicted fraction of vapor molecules approaches zero, but represents the free energy of a diatomic gas as this fraction approaches unity. Three new M-ANEOS input variables are required for the molecular vapor modification: a molecular binding energy, bond length, and number of internal degrees of freedom. The simulations here utilize M-ANEOS and the associated material constants for forsterite, kindly provided to us by H.J. Melosh and E. Pierazzo (e.g., Canup et al., 2002).

3.2. Initial conditions

We consider impactors and targets that contain 30% iron and 70% silicate (forsterite/dunite) by mass, differentiated into a core-mantle prior to the impact. We create objects in one of two ways. In the first, we collisionally generate the objects by colliding an iron projectile into a dunite target to produce a self-equilibrated and self-differentiated object (as in CA01). For a nearly Earth-mass target, this method produces temperatures ranging from 4000 K at the surface to as high as 20,000 K in the core, while temperatures in an \sim Mars mass impactor typically range from 2000 to 4000 K. Such temperatures would be similar to those expected for a planet having recently experienced another large impact or with inefficient cooling between impacts. We refer to simulations involving objects created in this manner as ‘hot starts.’

We also create initial objects with an iron core and a dunite mantle using a close-pack algorithm.⁷ Once particles are placed in a 3D-lattice, they are assigned initial

⁴ As the smoothing length of a particle is increased, its overall volume density is decreased, so that sparsely populated regions are necessarily low-density. Such a variable smoothing length method has been utilized subsequent to Cameron (1997), with earlier works using fixed smoothing lengths (Benz et al., 1986, 1987, 1989; Cameron and Benz, 1991).

⁵ For the object sizes considered here, material strength and fracture are unimportant, as are radiative processes for our simulated times (\sim a day).

⁶ In contrast, Tillotson treats mixed phase states by performing a smooth extrapolation in pressure between that of a solid and an ideal gas for an input (ρ, u) . This approach lacks any explicit treatment of phase changes or mixed phases, and does not maintain thermodynamic consistency (see discussion in Benz et al., 1989).

⁷ We note that by creating objects in this manner it is possible to set-up an unphysical initial condition that can cause ANEOS to fail to converge on a temperature for the inputted specific internal energy and density. For example, if the initial internal energy of particles in the center of a protoearth target is set artificially low (e.g., setting the object to a low uniform temperature that does not increase with depth), ANEOS can crash on inner particles that are under extremely high pressures but have apparently low specific internal energies. A typical failure mode is for ANEOS to iterate to lower and

temperatures with the assumption of an adiabatic and isentropic temperature profile, $dT/dP = \alpha T / \rho C_p$, where α is the coefficient of thermal expansion and C_p is the specific heat at constant pressure (e.g., Solomatov, 2000, and values therein), and a constant average density ρ , so that $P(r) = 2\pi G\rho^2(R-r)^2/3$, where R is the object radius and r is radial distance from the center. The objects are then “settled” (i.e., evolved for multiple dynamical times) during which time compression and additional heating occurs; after settling, the particle velocities are $\leq 1\%$ of the impact velocities to be considered in the actual impact simulations. For a surface temperature set to 2000 K, typical central temperatures are then ~ 3500 to 4500 K for the \sim Earth mass targets, and ~ 2500 to 3500 K for the impactors. We refer to simulations using such objects as “warm starts.”

Figure 1 shows density and temperature profiles for target protoearths created with both methods. The predicted internal densities are similar to those predicted for the Earth; e.g., a hydrostatic density model based on seismic wave velocities (de Pater and Lissauer, 2001, after Pieri and Dziewondski, 1999) estimates terrestrial mantle densities increasing with depth from ~ 3.3 g/cm³ at the edge of the upper mantle to ~ 5 g/cm³ near the core mantle boundary, with core densities increasing from ~ 10 to ~ 13 g/cm³ in the center of the Earth.

In standard SPH, a given particle’s density is defined by a summation over the contributions of the particle itself and all of its overlapping neighbors (Eq. (A.2)); this summed density is then sent to the equation of state, which treats the particle as a single pre-defined material type (iron or dunite in the simulations here). However, a particle’s overlapping neighbors are not necessarily of the same material type or reference density as the subject particle, so that as a result of SPH’s “smoothing,” an iron particle having dunite neighbors can have a reduced density relative to that it would have if surrounded by other iron particles (and vice versa for a silicate particle surrounded by iron particles). When objects are numerically settled prior to an impact simulation, such effects manifest themselves in a slight difference in SPH particle spacing at material boundaries (between the core and the mantle, and at the object’s surface) which have self-adjusted to create an equilibrated pressure profile. However, in the course of an impact simulation, such effects can potentially influence the “buoyancy” of iron particles in the mantle, particularly if differences in the interacting particle masses are large (Agnor and Asphaug, personal communication). Here for a given simulation, resolutions of the impactor and target mantle are set so that the particle masses

differ by less than a factor of 2 (in our highest resolutions simulations, somewhat more massive particles are used to describe the protoearth’s core). For the highest resolutions used here, particles in the protoearth’s mantle have typical smoothing lengths of $h \sim 300$ km.⁸

3.3. Analysis

Output from a given time step contains the position, velocity, specific internal energy, temperature, density, pressure, material state variable (e.g., solid or two-phase), object of origin (impactor vs. target) and matter type (i.e., dunite vs. iron) for each particle. The impacts are tracked for ~ 1 day of simulated time, at which point the protoearth has assumed an approximately oblate spheroid shape, and orbiting material has generally been sheared out into a disk.

The determination of whether a given particle at the end of a simulation is considered in the planet, orbiting, or escaping relies upon an iterative procedure (Appendix A of Canup et al., 2001). First, a guess is made for the mass contained in the central planet, M_P , and the planet’s oblateness, assuming a terrestrial density ($\rho_{\oplus} = 5.5$ g/cm³) and moment of inertia constant ($K_{\oplus} = 0.335$). These are used to compute the amounts of orbiting and escaping⁹ material and their associated angular momenta. For bound particles, an equivalent circular orbit of radius a_{eq} is computed from the magnitude of the particle’s angular momentum normal to the equatorial plane of the planet, L_z , with $L_z = m\sqrt{GM_P a_{\text{eq}}}$; those particles with a_{eq} greater than the equatorial radius of the planet are considered to be in the orbiting disk. The calculated escaping and disk masses and angular momenta then yield an improved estimate of the central planet’s mass and angular momentum (and thus, oblateness), and the process is repeated until convergence is achieved. Amounts of orbiting mass and angular momenta interior and exterior to the Roche limit are estimated by comparing a_{eq} to a_R .

The calculation of an equivalent circular orbit is consistent with an expectation that interactions among disk particles would lead to energy dissipation on a time scale short compared to that of angular momentum transport in the disk, since for a given angular momentum, a circular orbit is the lowest energy state. However, such a calculation can include as disk material SPH particles with periapses below the surface of the central planet, particularly if a significant portion of the orbiting mass is on high eccentricity orbits. We thus also compute equivalent keplerian orbits for the bound particles using their instantaneous \mathbf{r} and \mathbf{v} vectors, and compare an estimated disk mass computed by including only those particles with periapses above the equatorial radius of the

lower temperatures in an effort to provide a thermodynamical match to this low entropy situation, eventually reaching all the way to 0 K; sometimes this will occur in early stages of an impact, even when the objects were previously settled. We have identified two ways around such potential difficulties: (1) start with high initial uniform temperatures (e.g., Cameron and Benz, 1991, considered objects with temperatures of 4000 K), or (2) assign an initially more realistic temperature profile that increases with depth.

⁸ For a 3D simulation, $h \propto N^{1/3}$, so that even as the number of particles in a given simulation has increased by a factor of 40 from the earliest works (e.g., Benz et al., 1986, 1987), the linear resolution has increased only by a factor of ~ 3.4 .

⁹ Escaping material is defined as those particles with positive energies (i.e., $E/m = v^2/2 - GM_P/r > 0$).

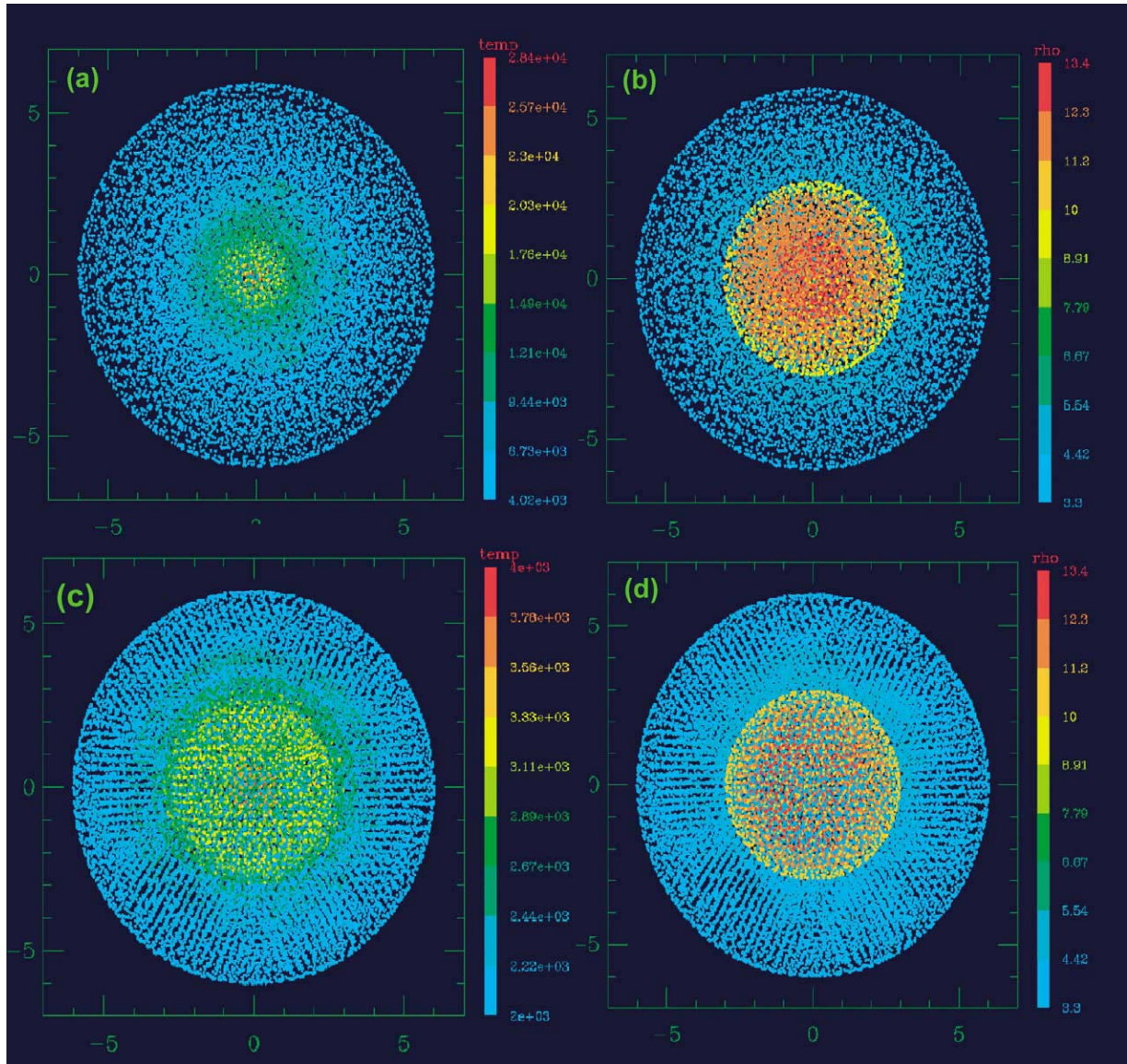


Fig. 1. Example initial target protoearths containing $0.89M_{\oplus}$. (a) Temperature in degrees K of all particles in an $N = 20,000$ protoearth created with the “hot start” method (see text); (b) density in g/cm^3 ; (c) temperature of all particles in an $N = 40,000$ particle protoearth created with the “warm start” method; (d) density in g/cm^3 for the object shown in (c).

Earth to that obtained from an equivalent circular orbit as described above.¹⁰ For the great majority of our simulations, these two methods of calculating the orbiting mass converge to within less than a few percent after 24 hours of simulated time.

The orbiting mass is itself a dynamic quantity (e.g., Cameron, 2000, his Fig. 6). Even after the system has settled into a central-planet and disk phase, the orbiting mass continues to generally decrease over time as particles undergo angular momentum exchange and some are scattered onto

the protoearth. With time, this behavior can be increasingly influenced by numerical effects due to the resolution scale of the disk, specifically the viscosity associated with SPH disk particles interacting over a radial distance determined by their smoothing lengths. An estimate of this effect can be made by relating the SPH artificial viscosity parameter $\bar{\alpha}$ (see Appendix A) to an equivalent disk viscosity through the relation

$$v_{\text{SPH}} \sim c_s h \bar{\alpha} / 8, \quad (2)$$

where c_s is sound speed and h is the typical disk smoothing length (e.g., Murray, 1996; Nelson et al., 1998). In our simulations, $\bar{\alpha} = 1.5$, and the resulting time scale for disk

¹⁰ Both methods for estimating orbiting mass ignore the role of pressure support for partially or fully vaporized material and so may underestimate the mass of orbiting material functionally in the disk.

particles is

$$\begin{aligned} \tau_{\text{SPH}} &\sim \frac{r^2}{v_{\text{SPH}}} \\ &\sim 10^2 \text{ hours} \left(\frac{r}{2R_{\oplus}} \right)^2 \left(\frac{0.5R_{\oplus}}{h} \right) \left(\frac{0.8 \text{ km/sec}}{c_S} \right). \end{aligned} \quad (3)$$

Spurious numerical angular momentum transport¹¹ in the disk and associated mass loss onto the central planet should be minimal so long as $\tau_{\text{simulated}} \ll \tau_{\text{SPH}}$; this condition is satisfied for our simulations for run times \sim a day (e.g., Fig. 5b).

4. Example potential moon-forming impacts

4.1. A disk-producing impact

Figure 2 shows a time series from an $N = 60,000$ particle simulation. Color scales with particle temperature, with red indicating particles with temperatures exceeding 6444 K. All particles in the 3D simulation are over-plotted, and viewed from above the plane of the impact. The impactor-to-total mass ratio is $\gamma = 0.13$, the total mass is $M_T = 1.019M_{\oplus}$, and the impact angular momentum is $L = 1.25L_{\text{EM}}$. The impactor and target were assumed to have zero relative velocity at infinity, so that their impact velocity, $v_{\text{imp}}^2 = v_{\infty}^2 + v_{\text{esc}}^2$, was just their mutual escape velocity

$$\begin{aligned} v_{\text{esc}}^2 &= 2G(M_{\text{imp}} + M_{\text{tar}})/(R_{\text{imp}} + R_{\text{tar}}) \\ &= 2GM_T^{2/3}(4\pi\rho/3)^{1/3}[\gamma^{1/3} + (1-\gamma)^{1/3}], \end{aligned} \quad (4)$$

or approximately 9.3 km/sec. Both objects were constructed in the “warm start” method described in Section 3.2. The scaled impact parameter was $b' = 0.73$, where we define $b' \equiv L/L_{\text{graz}} \equiv \sin \xi$, where ξ is the angle of the trajectory to the local surface normal, and L_{graz} is the angular momentum of a grazing, $b' = 1$ impact, which for $v_{\text{imp}} = v_{\text{esc}}$ is:

$$L_{\text{graz}} = [3/(4\pi\rho)]^{1/6} \sqrt{2G} f(\gamma) M_T^{5/3}. \quad (5)$$

Here ρ is the target/impactor density and $f(\gamma) \equiv \gamma(1-\gamma) \times [\gamma^{1/3} + (1-\gamma)^{1/3}]^{1/2}$ (e.g., Canup et al., 2001).

After the initial oblique impact and initiation of a shock wave in both objects (Fig. 2a at 6 minutes), a portion of

the impactor that, as a result of its physical offset, avoided colliding directly with the protoearth is sheared off and continues forward ahead of the impact site, with some highly heated material from the impact interface below and behind it (Fig. 2b at 20 minutes). After about 50 minutes, the highly distorted form of the impactor extends to a distance of about 3 to 3.5 Earth radii (Fig. 2c), and the target and the inner portions of the impactor begin to rotate ahead of the distant portions of the impactor. Both the inner orbiting impactor material and the wave/bulge on the surface of the protoearth that forms after about 80 minutes (Fig. 2d) lead ahead of the outer portions of the impactor, providing a positive torque; after about 2 hours (Fig. 2e), the latter bulge has propagated about two-thirds of the way around the planet from the initial impact site, while the most distant portions of the impactor, now at about 6 Earth radii from the planet’s center, begin to gravitationally self-contract. An “arm” of impactor material has formed extending from this distant clump to the surface of the Earth; within this arm is the sheared iron core of the impactor. In the 3 to 5 hour time frame, the radially inner portions of the impactor (composed primarily of the impactor’s core), gravitationally contract into a semi-coherent object that has an observable counterclockwise spin (Fig. 2f), and which re-collides with the planet after about 6 hours (Fig. 2g). At this point, most of the impactor’s iron has been removed from orbit. The outer clump of the impactor—composed entirely of material from the impactor’s mantle—eventually makes an orbital pass with a perigee just above the surface of the protoearth, and is sheared into a long, spiral arm like structure (Figs. 2i–2j), which finally breaks up into multiple smaller clumps (Fig. 2k). The last frame (Fig. 2l) is the system at 27 hours viewed on edge, shown with a higher temperature scale (with red now indicating particle temperatures in excess of 9110 K).

At the end of the Fig. 2 impact, the bound planet-disk system has an angular momentum of $L_F = 1.18L_{\text{EM}}$, the mass of the central planet is $0.994M_{\oplus}$, and its rotational day is about 4.6 hours with $J_2 \approx 0.03$. A total mass of $M_e = 0.41M_L$ has escaping orbits. The disk, described by 2203 particles, contains $1.62M_L$, with $0.92M_L$ having equivalent circular orbits exterior to the Roche limit; the total angular momentum in orbiting material is $L_D = 0.31L_{\text{EM}}$. Using Eq. (1) with $(M_{\text{esc}}/M_D) = 0.05$, the predicted mass of the satellite that would accrete from this disk is $1.4M_L$.

Of the material with equivalent orbits exterior to a_R , 80% of the mass originated in the impactor, 24% is vapor,¹² and 1.9% is iron. For material with equivalent orbits interior

¹¹ Two potential modes for the viscous evolution of a protolunar disk have been proposed. The first is driven by an instability-enhanced viscosity in a Roche-interior disk of condensates (Ward and Cameron, 1978; see also Takeda and Ida, 2001), which when applied to a lunar mass of disk material leads to predicted disk spreading times \sim months. In the second, the viscosity is limited by the radiation budget of the disk, implying much longer disk spreading times \sim 50 to 100 years (Thompson and Stevenson, 1988). From basic energy arguments for a \sim lunar mass disk, the latter is more appropriate. But for the resolutions utilized here, the viscosity in Eq. (2) is orders-of-magnitude larger (and the associated numerical spreading time is orders-of-magnitude shorter) than any physical estimate of the protolunar disk viscosity.

¹² Vapor fractions are computed by summing (1) the particle masses in the ANEOS “two-phase” state multiplied by the predicted vapor mass fraction for each particle and (2) the entire particle masses for those particles in a single phase vapor state. For dunite, (1) occurs for particles with $2205 \text{ K} < T < 6034 \text{ K}$ and with densities $< 3.1187 \text{ g/cm}^3$; typically the majority of the disk material is in this two-phase state.

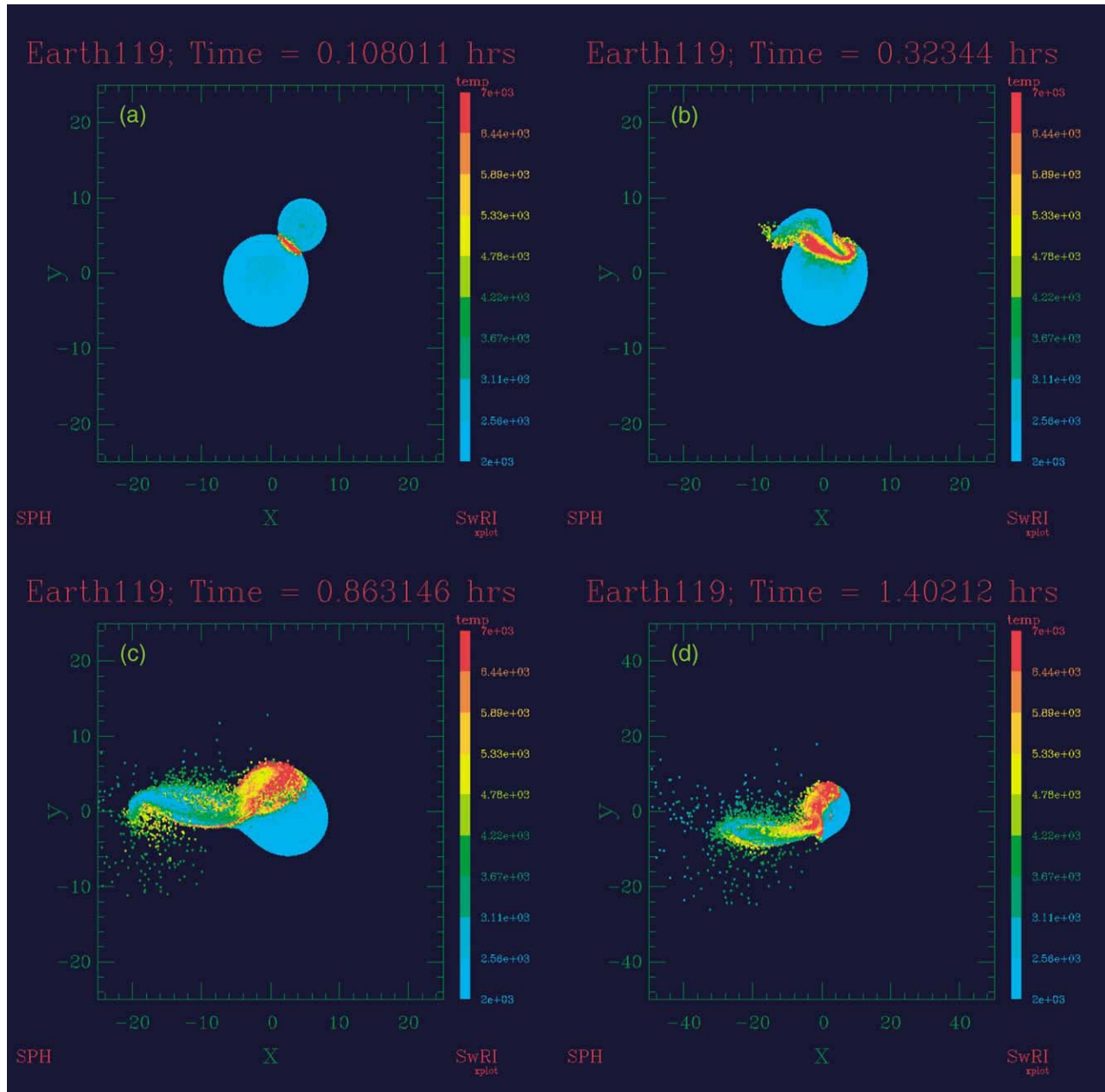


Fig. 2. Time series of an impact with $N = 60,000$, $\gamma = 0.13$, $v = v_{\text{esc}}$, and $b' = 0.730$. Times are shown in hours and color scales with particle temperature in degrees K; frames (a) through (k) are looking down onto the plane of the impact, with particles with $T > 6440$ K shown in red. Distances are shown in units of 1000-km. Frame (i) is the final state viewed on-edge; here the temperature scale has been shifted so that red corresponds to $T > 9110$ K.

to a_R , 85% is from the impactor, 22% is vapor, and 9.1% is iron. Of all of the material (escaping and bound), 23% is predicted to be in the vapor state. This vapor fraction is similar to that found by estimating the degree of entropy production during an irreversible shock produced by the initial impact. Stevenson (1987, his Fig. 4) estimated the entropy change and peak shock pressure as a function of impact velocity, together with resulting liquid–vapor fractions during an assumed isentropic pressure release from this peak shock state. E.g., for an impact velocity of 10 km/sec, and assuming a normal impact, an approximately 20% vapor/80% liquid mixture was predicted at $T \sim 4000$ K start-

ing from a peak pressure comparable to that found here ($\sim 3 \times 10^6$ bar at a time intermediate to that shown in Figs. 2a and 2b).

Figures 3a–3b show a mapping of the peak temperature achieved by each particle during the simulation onto the original figures of the impactor and target. Not surprisingly, regions of highest peak temperatures in both objects are located at the impact interface of the initial collision (e.g., bottom left quadrant of the impactor in Fig. 3b), in addition to the impactor material involved in the front face of the second collision, which here appears as bands crossing the impactor from the bottom left to upper right.

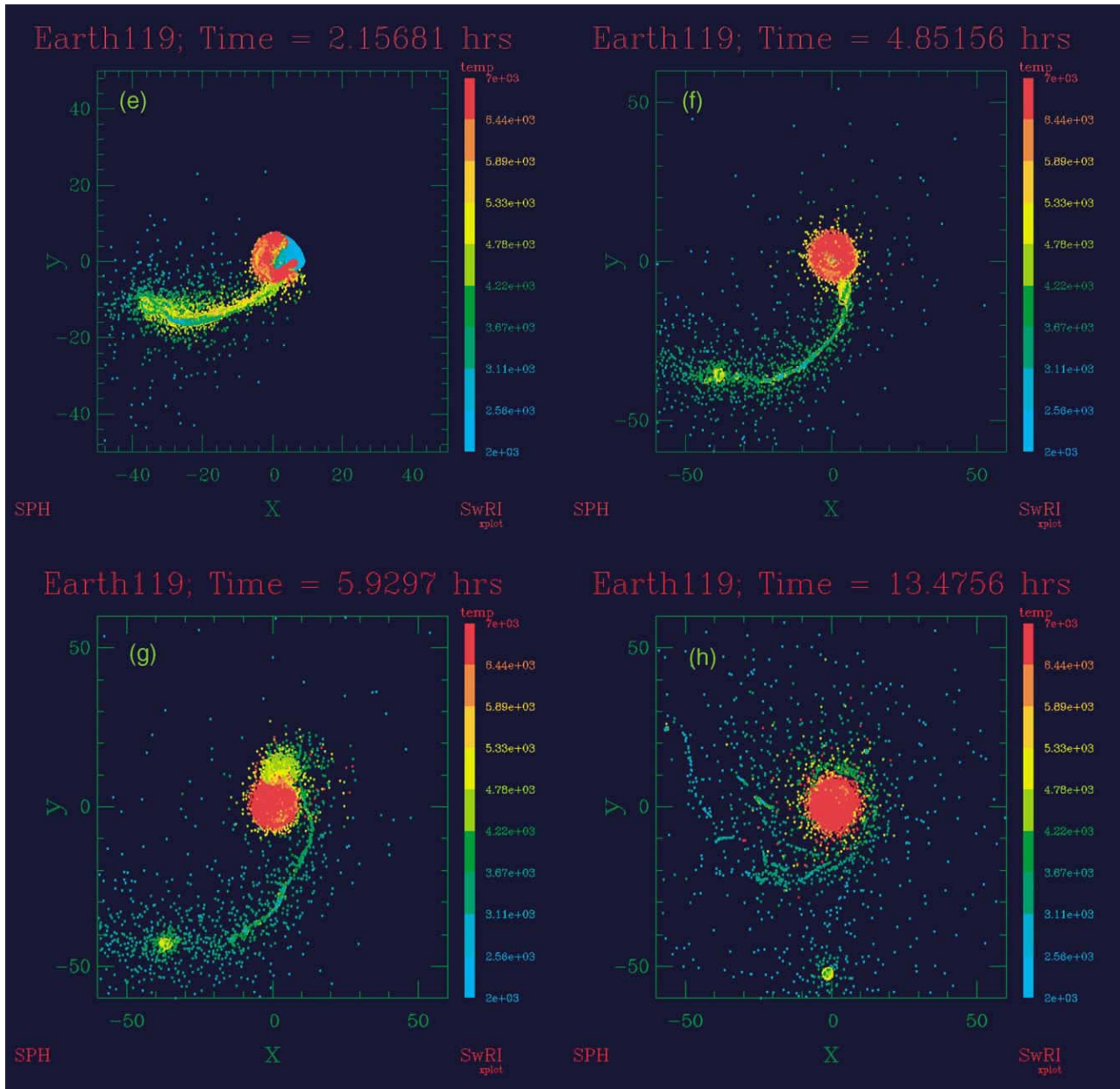


Fig. 2. Continued.

Figures 3c–3e show a mapping of final particle state (escape, orbiting, or in planet) onto the original objects (Figs. 3c–3d), and the objects just after the initial impact (Fig. 3e); here yellow–green particles are those that comprise the final disk, red particles escape, and blue particles are accreted by the planet. Most of the material that ends up in orbit originates from the leading face of the impactor that was just exterior (e.g., at greater radial distance from the center of the target) to the primary impact interface. A region of escaping particles on the impactor just below this region is associated with the front edge of the initial impact site, which from Figs. 3a–3b is shown to be highly-heated/vaporized material; this is likely a result of “jetting” (e.g., Vickery and Melosh, 1987) from the initial oblique im-

pact. Figure 3f shows the instantaneous particle temperatures at the time step shown in Fig. 3e; only particles within a 4000-km slice centered on the $z = 0$ plane are plotted, together with vectors whose length is proportional to particle velocity. From the velocity vectors in Fig. 3f, it can be seen that the leading material in Fig. 3e that eventually escapes has been significantly accelerated as a result of the initial impact (e.g., the highest magnitude velocity at this time is ~ 14 km/sec, vs. an impact velocity ~ 9 km/sec).

Comparison of Fig. 3d with the temperature map in Fig. 3b shows that the impactor material that eventually comprises the orbiting disk is primarily the *least* thermally heated of all of the material originally in the impactor, having for the most part avoided direct impact with the pro-

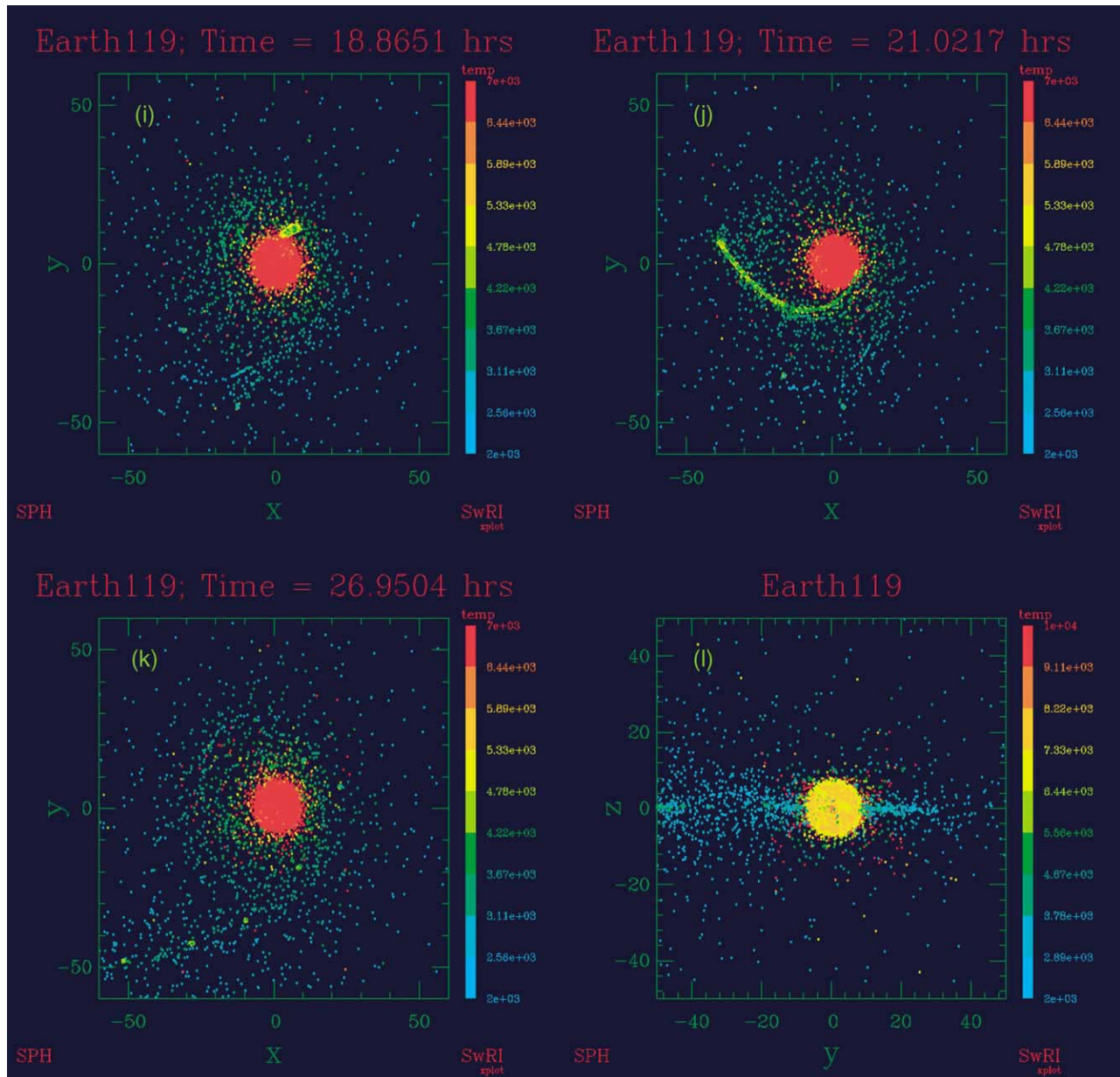


Fig. 2. Continued.

toearth. This is seemingly at odds with the view that would directly associate orbital emplacement with material having experienced the greatest degree of heating/vaporization (e.g., Cameron and Ward, 1976; Vickery and Melosh, 1987), arguing instead for the importance of impact geometry and gravitational torques. However, the escaping vaporized material seen in Figs. 3e and 3f may affect neighboring material via pressure gradients that helps the latter to eventually achieve orbit. This issue merits further investigation.

Figures 4a–4c show properties of a 2000-km slice centered on the equatorial plane of the final, post-impact protoearth. Comparison of Fig. 4a (final temperature) with Fig. 4b (impactor vs. target origin of the material) shows that

the impactor material incorporated into the final protoearth is more severely heated on average than the target material, most notably a ~ 7000 – 8000 K silicate atmosphere of primarily impactor origin material envelopes the final protoearth (also seen in Fig. 2l). Figure 4c shows iron vs. silicate composition; from comparison with Fig. 4a, the hottest material in the planet is the impactor iron, most of which has accumulated around the outer rim of the original target core. Figure 4d shows the disk and protoearth, including all particles, with red and blue indicating iron and dunite, respectively.

Figure 5a shows computed keplerian orbital elements for the disk particles; these must be viewed as only broadly representative of the initial debris distribution since they do

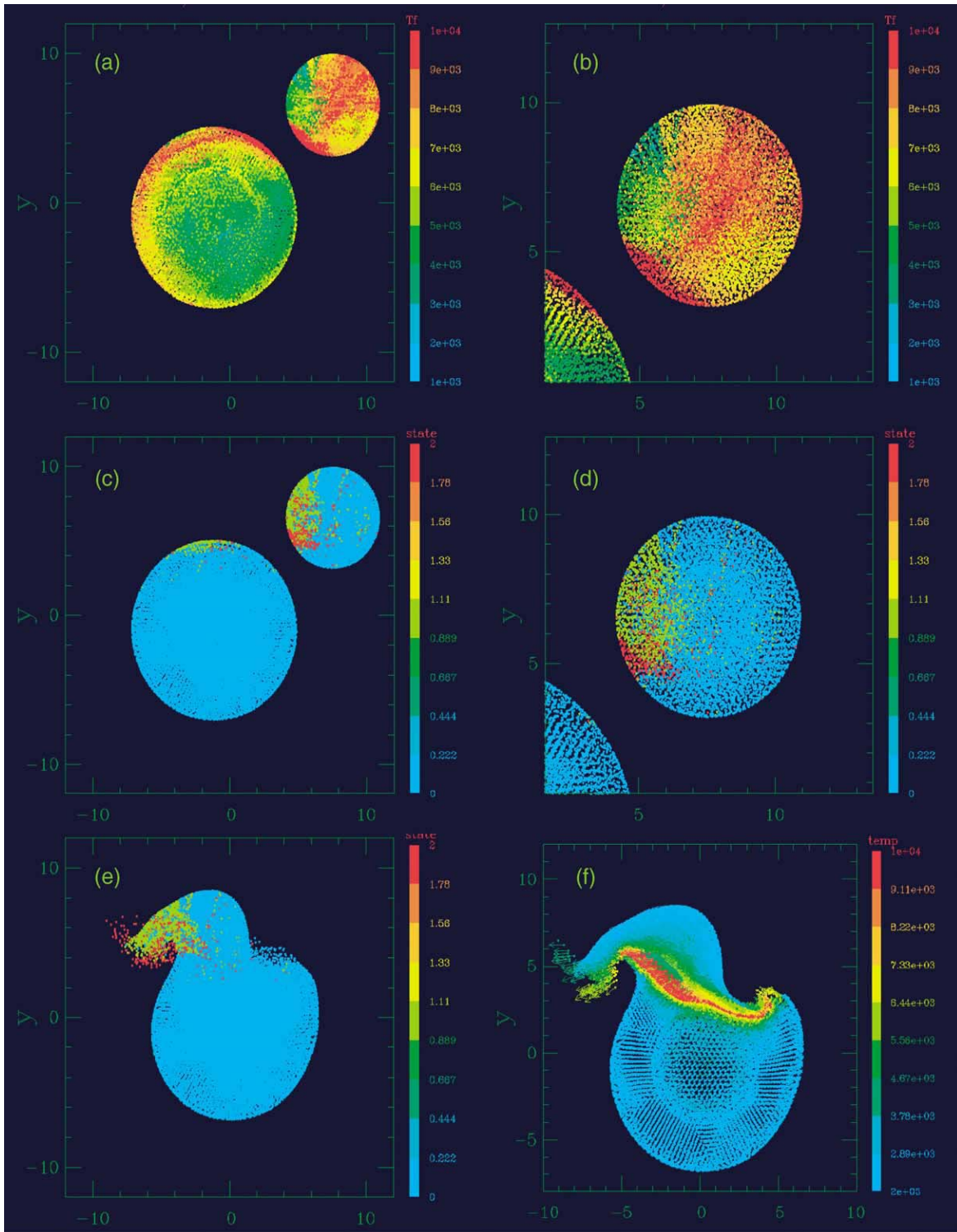


Fig. 3. Mapping of impact quantities onto original figures of target and impactor. (a) Peak particle temperatures experienced during impact shown in Fig. 1; color scales with temperature in degrees K with red for $T > 9000$ K; (b) same as (a), close-up on impactor; (c) mapping of final particle states; yellow-green particles end up in the orbiting disk, red escape the system, and blue end up in the protoearth; (d) same as (c), close-up on impactor; (e) mapping of final particle states onto time step shown in Fig. 2b, same color scale as (c) and (d); (f) instantaneous particle temperatures within a 4000-km slice centered on the $z = 0$ plane for the time step shown in (e). The vectors are proportional to the particle velocity magnitude.

not account for pressure support. While a majority of the orbiting material has equivalent circular orbits exterior to a_R , most orbits have periaapses interior to the Roche limit.

This means that Roche exterior clumps may undergo orbital passes within a_R , and are then likely to be tidally disrupted in their immediate post-impact evolution (e.g., Cameron,

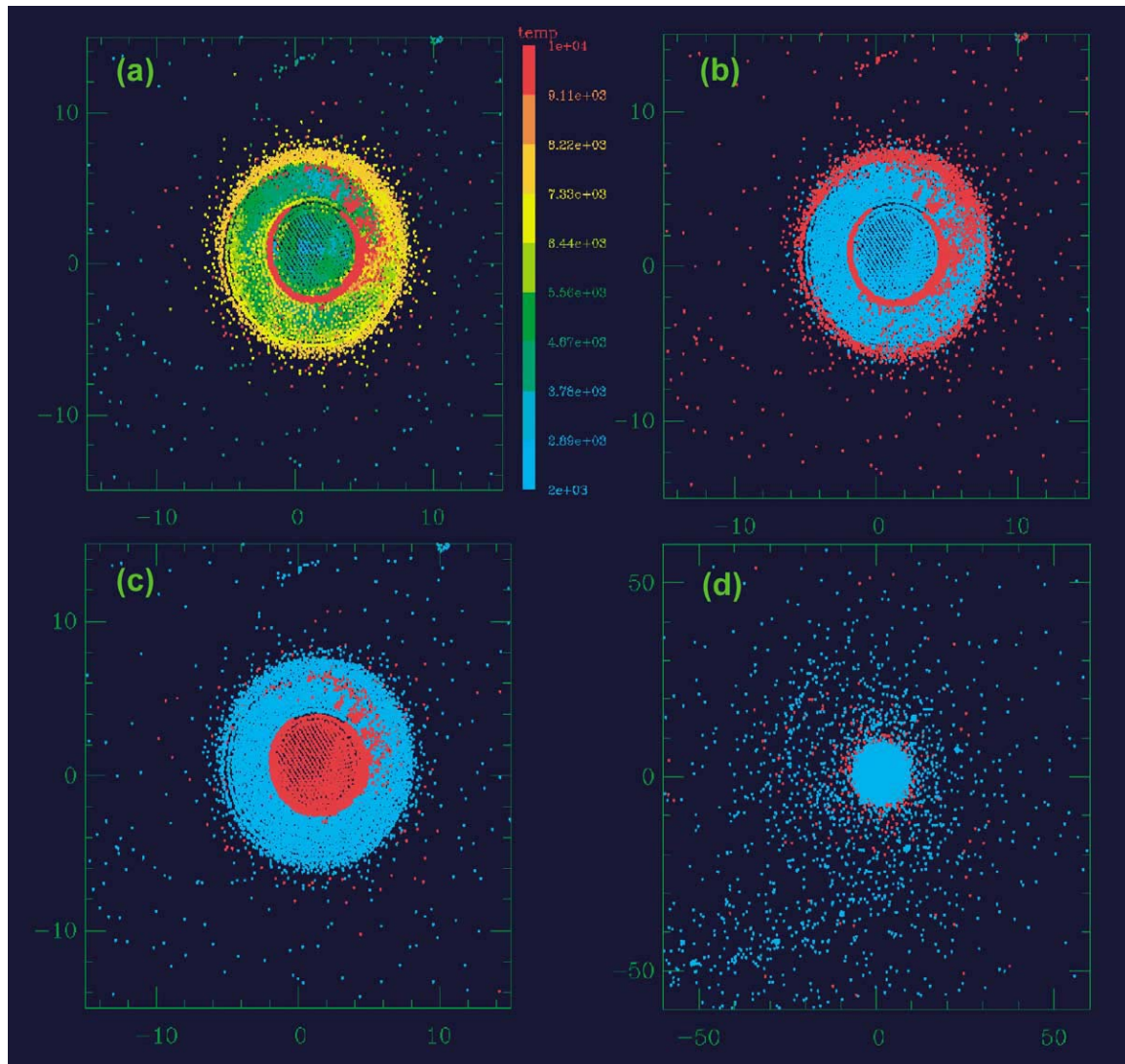


Fig. 4. Post-impact state of protoearth and disk from simulation shown in Fig. 2. (a) Temperatures within a 2000-km thick slice through the protoearth, parallel with and centered on the equatorial plane of the planet; (b) same slice as shown in (a), but here color scales with the source object of the material, with red particles originating from the impactor and blue from the target; (c) same slice as in (a), but color scales with material type, with iron particles in red and dunite particles in blue; (d) the entire protoearth and disk, with color scaling with material type (iron vs. dunite) as in (c).

2000). Figure 5b shows numerical spreading times calculated for individual disk particles from Eq. (3); the shortest characteristic times are ~ 30 hours.

Figure 6 shows the final particle temperatures vs. instantaneous radial position for dunite (black) vs. iron (red). In the final protoearth, rock temperatures are in the 2000 to 10,000 K range, with iron from the impactor reaching much higher temperatures of tens-of-thousands of degrees K. The disk rock has temperatures ranging from 2500 to 5000 K; some of the disk iron is significantly hotter, with temperatures in excess of 10,000 K in the inner disk.

4.2. A disk-moon producing impact

Figure 7 shows an $N = 120,000$ particle simulation with a somewhat larger impactor with $\gamma = 0.15$, and a slightly reduced total mass of $M_T = 0.95M_\oplus$. The impact angular

momentum is $L = 1.26L_{EM}$, $v_{imp} = v_{esc}$, and $b' = 0.726$. A very similar impact sequence results as in Fig. 2, with an inner clump composed primarily of the iron core of the impactor undergoing a second impact with the protoearth (Fig. 7b). However, in this case, the outer clump remains largely intact on a Roche-exterior orbit, yielding a final moon-disk system.

At the end of the Fig. 7 impact, the bound planet-disk system has an angular momentum of $L_F = 1.21L_{EM}$, the mass of the central planet is $0.924M_\oplus$, and its rotational day is about 4.2 hours with $J_2 \approx 0.035$. A total mass of $M_e = 0.28M_L$ has escaping orbits. The orbiting disk, described by 4800 particles, contains $1.82M_L$, 2.2% iron, and an angular momentum of $L_D = 0.363L_{EM}$. Of the mass having equivalent orbits exterior to a_R ($1.42M_L$), 86% originated in the impactor, 12% is vapor, and $< 1\%$ is iron. For

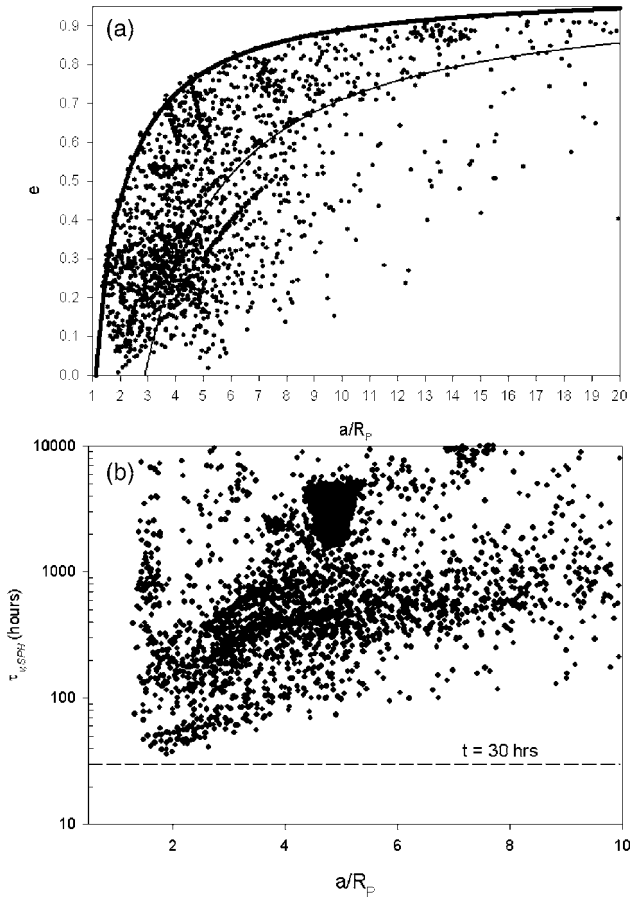


Fig. 5. Properties of the disk particles at the end of the simulation shown in Fig. 2. (a) Particle eccentricity vs. semi-major axis (computed assuming a keplerian orbit); curves of constant periapse are shown at 1.1 planetary radii (thick line) and the Roche limit (thin line); (b) numerical viscous spreading timescales from Eq. (3) computed for individual orbiting particles as a function of semi-major axis.

material with equivalent orbits interior to $a_R(0.4M_L)$, 80% is from the impactor, 16% is vapor, and 9.1% is iron. Using Eq. (1) with $(M_{\text{esc}}/M_D) = 0.05$, the predicted mass of the satellite that would accrete from this disk is equal to the total disk mass. This is because there is sufficient angular momentum in the disk to have all of the disk mass orbiting in a single moon with $a = 1.2a_R$. However, this case is an example of a high angular momentum disk that exceeds the range considered to date by accretion simulations; for such a disk the assumptions of $(M_{\text{esc}}/M_d) = 0.05$ and $a = 1.2a_R$ may no longer be valid (e.g., Kokubo et al., 2000, Fig. 9).

We estimate the largest clump (Fig. 7e) contains 61% of a lunar mass and is described by about 1700 SPH particles. The tendency for the formation of large intact clumps as a direct result of the impact has been found previously (e.g., Cameron and Benz, 1991; Cameron, 2000). For example, the $N = 3000$ particle simulation shown in Cameron and Benz (1991, their Fig. 2 and run DE11) had $\gamma = 0.14$, $L = 1.3L_{\text{EM}}$, $v_{\text{imp}} = v_{\text{esc}}$, and $b' = 0.74$, and produced a disk containing 1.4 lunar masses, including a single clump

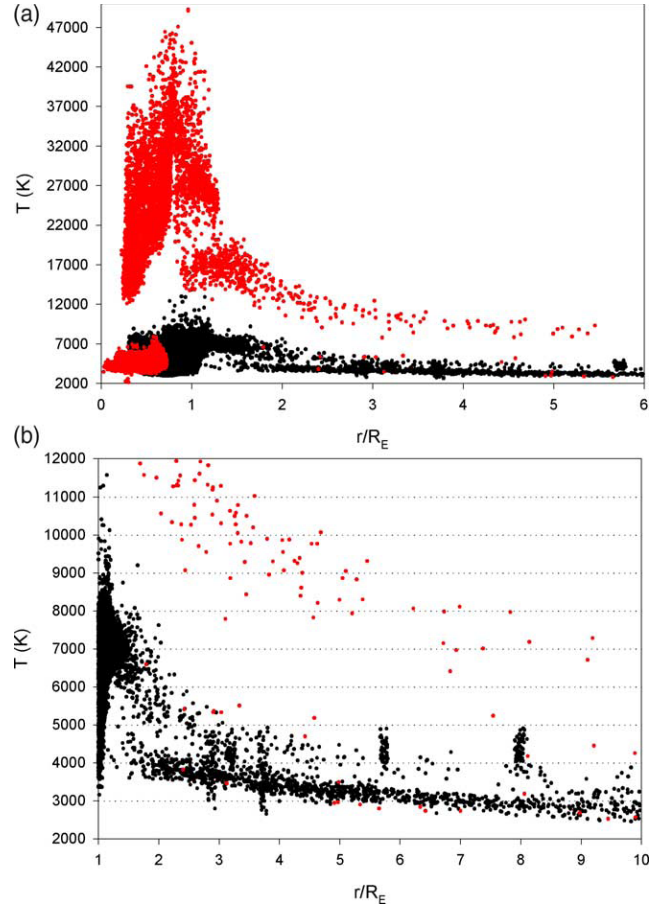


Fig. 6. Temperature vs. instantaneous radial position for all of the particles at the end of the simulation in Fig. 2. Red particles are iron; black are dunite.

containing $0.86M_L$ described by 32 SPH particles. Although the time sequence in Fig. 7 has a quite different morphology than that of DE11, the basic similarity in outcomes is striking given the nearly two orders of magnitude difference in disk resolution. Similar outcomes to that of Fig. 7 were also found for some of the medium resolution runs in CA01 utilizing the Tillotson EOS. Thus the direct formation of large clumps for certain impacts has been observed over a wide range in resolution, and for all of the previously utilized equations of state (ANEOS, M-ANEOS, and Tillotson). However, as a cautionary reminder we note that these results have all been derived using SPH, which as a method is known to be capable of producing spurious clumping (e.g., Imaeda and Inutsuka, 2002).

4.3. Properties of successful impacts

Table 1 lists properties of 47 “successful” lunar-forming impacts, defined as those that leave iron-poor disks with a predicted satellite mass $\geq M_L$ from Eq. (1). The successful impacts involved impactor-to-total mass ratios ranging from 0.11 to 0.15, an impact occurring very late in Earth’s accretion with $M_T \geq 0.95M_{\oplus}$, impact velocities of $1.0 \leq (v_{\text{imp}}/v_{\text{esc}}) \leq 1.1$, and impact parameters in the range

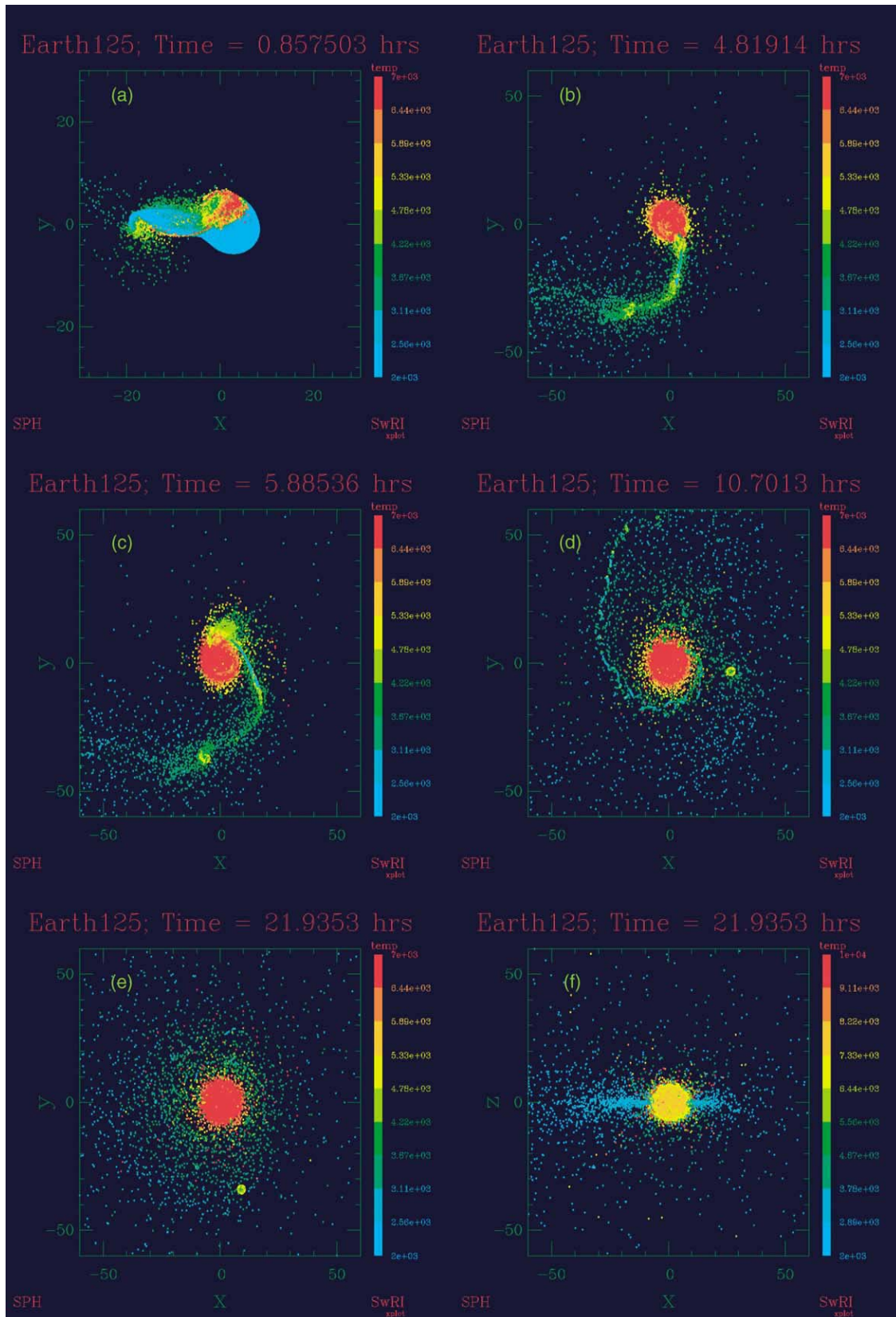


Fig. 7. Time series of an impact with $N = 120,000$, $N_{\text{imp}} = 0.15$, $v = v_{\text{esc}}$, and $b' = 0.726$. Times are shown in hours and color scales with particle temperature in degrees K; frames (a) through (e) are looking down onto the plane of the impact, with particles with $T > 6440$ K shown in red. Distances are shown in units of 1000-km. Frame (f) is the final state viewed on-edge; here the temperature scale has been shifted so that red corresponds to $T > 9110$ K. The large orbiting clump in (d) and (e) contains about 60% of a lunar mass and is represented by ~ 1700 particles.

$0.67 \leq b' \leq 0.76$ (corresponding to a range in impact angle of 42 to 50 degrees). Of these, about three-fourths produced disks with only small clumps as in Fig. 2 or no significant clumps, while about 25% left a disk and a large moon/clump as in Fig. 7; the second outcome was found at all of the resolutions considered (20 to 120 K), although in some cases

altering the resolution for otherwise identical impact conditions produced a change in the disk vs. disk-moon result. The disks contain material that is at least 70% impactor in origin, with disk vapor fractions ranging from 10 to 30%; the final system angular momenta, L_F , are typically 10 to 20% higher than that of the current Earth–Moon system.

Table 1

Results from 47 potential lunar forming impacts, defined as those that yield predicted satellite masses $\geq M_L$, contain $< 10\%$ iron by mass in orbit, and $< 5\%$ iron by mass for disk material with equivalent orbits exterior to the Roche limit

| $N/10^3$ | γ | $N_{\text{imp}}/v_{\text{esc}}$ | b' | L/L_{EM} | M_e/M_L | M_D/M_L | L_D/L_{EM} | M_{Fe}/M_D | M_v/M_D | M_{imp}/M_D | M_D ($a > a_R$) | M_{Fe}/M_D ($a > a_R$) | L_F/L_{EM} | M_M/M_L |
|------------------|----------|---------------------------------|-------|-------------------|-----------|-----------|---------------------|---------------------|-----------|----------------------|------------------------|--------------------------------------|---------------------|-----------|
| 30 | 0.11 | 1.00 | 0.728 | 1.07 | 0.46 | 1.19 | 0.23 | 0.03 | 0.18 | 0.81 | 0.57 | 0.04 | 1.00 | 1.00 |
| 30 | 0.11 | 1.00 | 0.738 | 1.09 | 0.38 | 1.32 | 0.27 | 0.02 | 0.15 | 0.81 | 0.96 | 0.00 | 1.03 | 1.23 |
| 30 | 0.11 | 1.00 | 0.750 | 1.10 | 0.54 | 1.25 | 0.24 | 0.07 | 0.23 | 0.84 | 0.73 | 0.02 | 0.99 | 1.07 |
| 30 | 0.11 | 1.00 | 0.762 | 1.12 | 0.61 | 1.04 | 0.23 | 0.10 | 0.26 | 0.84 | 0.73 | 0.04 | 1.00 | 1.04 |
| 30 | 0.13 | 1.00 | 0.723 | 1.24 | 0.42 | 1.33 | 0.26 | 0.07 | 0.28 | 0.75 | 0.81 | 0.03 | 1.16 | 1.17 |
| 20 ^h | 0.13 | 1.00 | 0.723 | 1.24 | 0.36 | 1.27 | 0.27 | 0.04 | 0.25 | 0.78 | 0.92 | 0.00 | 1.18 | 1.27 |
| 30 | 0.13 | 1.00 | 0.724 | 1.24 | 0.35 | 1.46 | 0.30 | 0.05 | 0.23 | 0.79 | 0.92 | 0.02 | 1.19 | 1.38 |
| 30 ^c | 0.13 | 1.00 | 0.730 | 1.25 | 0.27 | 1.41 | 0.31 | 0.04 | 0.15 | 0.81 | 1.17 | 0.01 | 1.20 | 1.41 |
| 30 | 0.13 | 1.00 | 0.730 | 1.25 | 0.34 | 1.51 | 0.31 | 0.04 | 0.16 | 0.84 | 1.17 | 0.03 | 1.19 | 1.49 |
| 60 | 0.13 | 1.00 | 0.730 | 1.25 | 0.71 | 1.62 | 0.31 | 0.05 | 0.23 | 0.82 | 0.92 | 0.02 | 1.18 | 1.38 |
| 120 | 0.13 | 1.00 | 0.730 | 1.25 | 0.51 | 1.59 | 0.30 | 0.05 | 0.20 | 0.77 | 0.89 | 0.03 | 1.16 | 1.28 |
| 30 | 0.13 | 1.00 | 0.733 | 1.26 | 0.71 | 1.41 | 0.31 | 0.02 | 0.15 | 0.86 | 1.14 | 0.00 | 1.10 | 1.41 |
| 20 ^h | 0.13 | 1.00 | 0.733 | 1.26 | 0.54 | 1.09 | 0.24 | 0.03 | 0.22 | 0.79 | 0.83 | 0.01 | 1.14 | 1.09 |
| 30 | 0.13 | 1.00 | 0.735 | 1.26 | 0.41 | 1.41 | 0.31 | 0.04 | 0.17 | 0.83 | 1.10 | 0.01 | 1.19 | 1.41 |
| 30 | 0.13 | 1.00 | 0.740 | 1.27 | 0.43 | 1.58 | 0.35 | 0.04 | 0.17 | 0.85 | 1.26 | 0.01 | 1.19 | 1.58 |
| 60 | 0.13 | 1.00 | 0.740 | 1.27 | 0.36 | 1.59 | 0.34 | 0.03 | 0.17 | 0.87 | 1.20 | 0.01 | 1.21 | 1.59 |
| 120 | 0.13 | 1.00 | 0.740 | 1.27 | 0.45 | 1.54 | 0.31 | 0.04 | 0.21 | 0.80 | 1.02 | 0.01 | 1.19 | 1.44 |
| 20 ^h | 0.13 | 1.00 | 0.744 | 1.28 | 0.35 | 1.62 | 0.35 | 0.03 | 0.10 | 0.88 | 1.37 | 0.01 | 1.21 | 1.62 |
| 30 | 0.13 | 1.00 | 0.745 | 1.28 | 0.41 | 1.33 | 0.30 | 0.06 | 0.24 | 0.89 | 1.05 | 0.01 | 1.21 | 1.33 |
| 30 | 0.13 | 1.00 | 0.750 | 1.28 | 0.67 | 1.31 | 0.28 | 0.08 | 0.21 | 0.86 | 0.94 | 0.03 | 1.14 | 1.31 |
| 30 | 0.13 | 1.00 | 0.756 | 1.29 | 0.86 | 1.12 | 0.23 | 0.09 | 0.26 | 0.83 | 0.74 | 0.03 | 1.11 | 1.09 |
| 20 ^h | 0.13 | 1.00 | 0.756 | 1.29 | 0.72 | 1.09 | 0.23 | 0.07 | 0.28 | 0.84 | 0.79 | 0.01 | 1.15 | 1.09 |
| 20 ^h | 0.13 | 1.02 | 0.703 | 1.23 | 0.42 | 1.67 | 0.30 | 0.05 | 0.14 | 0.82 | 0.59 | 0.03 | 1.16 | 1.12 |
| 60 | 0.13 | 1.02 | 0.730 | 1.28 | 0.39 | 1.82 | 0.37 | 0.03 | 0.13 | 0.86 | 1.47 | 0.02 | 1.22 | 1.71 |
| 20 ^h | 0.13 | 1.05 | 0.718 | 1.29 | 0.61 | 1.62 | 0.33 | 0.06 | 0.11 | 0.84 | 1.19 | 0.02 | 1.19 | 1.58 |
| 30 | 0.13 | 1.05 | 0.730 | 1.31 | 0.58 | 1.68 | 0.36 | 0.03 | 0.12 | 0.86 | 1.29 | 0.00 | 1.21 | 1.68 |
| 20 ^h | 0.13 | 1.05 | 0.730 | 1.31 | 0.54 | 1.57 | 0.36 | 0.06 | 0.12 | 0.87 | 1.11 | 0.04 | 1.21 | 1.57 |
| 60 | 0.13 | 1.05 | 0.730 | 1.31 | 0.70 | 1.76 | 0.33 | 0.06 | 0.13 | 0.85 | 0.98 | 0.03 | 1.19 | 1.43 |
| 120 | 0.13 | 1.05 | 0.730 | 1.31 | 0.79 | 1.74 | 0.32 | 0.05 | 0.12 | 0.83 | 0.91 | 0.03 | 1.17 | 1.35 |
| 20 ^h | 0.13 | 1.10 | 0.714 | 1.34 | 0.98 | 1.83 | 0.35 | 0.09 | 0.08 | 0.87 | 1.14 | 0.05 | 1.15 | 1.57 |
| 30 | 0.13 | 1.10 | 0.730 | 1.37 | 1.03 | 1.33 | 0.30 | 0.09 | 0.16 | 0.81 | 0.88 | 0.03 | 1.18 | 1.33 |
| 30 ^s | 0.15 | 1.00 | 0.693 | 1.20 | 0.30 | 1.33 | 0.24 | 0.05 | 0.30 | 0.73 | 0.76 | 0.01 | 1.17 | 1.07 |
| 30 ^s | 0.15 | 1.00 | 0.706 | 1.22 | 0.30 | 1.52 | 0.29 | 0.03 | 0.23 | 0.77 | 1.05 | 0.01 | 1.17 | 1.38 |
| 30 ^s | 0.15 | 1.00 | 0.719 | 1.24 | 0.37 | 1.53 | 0.32 | 0.01 | 0.19 | 0.85 | 1.25 | 0.00 | 1.17 | 1.53 |
| 30 ^s | 0.15 | 1.00 | 0.726 | 1.26 | 0.31 | 1.61 | 0.34 | 0.04 | 0.20 | 0.87 | 1.31 | 0.02 | 1.21 | 1.61 |
| 120 ^s | 0.15 | 1.00 | 0.726 | 1.26 | 0.28 | 1.83 | 0.36 | 0.02 | 0.13 | 0.85 | 1.42 | 0.00 | 1.21 | 1.83 |
| 30 ^s | 0.15 | 1.00 | 0.732 | 1.27 | 0.53 | 1.42 | 0.29 | 0.10 | 0.23 | 0.89 | 1.07 | 0.05 | 1.17 | 1.42 |
| 30 ^s | 0.15 | 1.00 | 0.737 | 1.28 | 0.65 | 1.31 | 0.26 | 0.08 | 0.25 | 0.87 | 0.88 | 0.02 | 1.15 | 1.29 |
| 30 ^s | 0.15 | 1.00 | 0.743 | 1.28 | 0.69 | 1.27 | 0.25 | 0.04 | 0.28 | 0.84 | 0.87 | 0.01 | 1.14 | 1.21 |
| 30 ^s | 0.15 | 1.02 | 0.726 | 1.28 | 0.41 | 1.52 | 0.32 | 0.07 | 0.21 | 0.88 | 1.18 | 0.03 | 1.22 | 1.52 |
| 30 ^s | 0.15 | 1.02 | 0.730 | 1.29 | 0.43 | 1.47 | 0.31 | 0.05 | 0.27 | 0.85 | 1.11 | 0.02 | 1.23 | 1.47 |
| 30 ^s | 0.15 | 1.05 | 0.671 | 1.22 | 0.92 | 1.34 | 0.26 | 0.04 | 0.23 | 0.73 | 0.85 | 0.02 | 1.09 | 1.23 |
| 30 ^s | 0.15 | 1.05 | 0.693 | 1.26 | 0.56 | 1.82 | 0.34 | 0.05 | 0.15 | 0.80 | 1.06 | 0.05 | 1.17 | 1.56 |
| 120 ^s | 0.15 | 1.05 | 0.693 | 1.26 | 0.51 | 2.14 | 0.37 | 0.03 | 0.12 | 0.78 | 0.88 | 0.02 | 1.18 | 1.60 |
| 30 ^s | 0.15 | 1.05 | 0.726 | 1.32 | 0.60 | 1.59 | 0.32 | 0.07 | 0.22 | 0.76 | 1.09 | 0.03 | 1.22 | 1.59 |
| 30 ^s | 0.15 | 1.05 | 0.732 | 1.33 | 0.95 | 1.24 | 0.25 | 0.10 | 0.25 | 0.84 | 0.80 | 0.04 | 1.14 | 1.24 |
| 30 ^s | 0.15 | 1.05 | 0.737 | 1.34 | 0.91 | 1.40 | 0.26 | 0.08 | 0.30 | 0.81 | 0.82 | 0.04 | 1.16 | 1.21 |

Results are grouped by impactor-to-total mass ratio, impact velocity relative to escape velocity, and impact parameter. In all cases, the total colliding mass = $1.109M_{\oplus}$ except, ^s where $M_T = 0.95M_{\oplus}$. Runs utilized “warm starts” with surface temperatures set to 2000 K except those marked ^h(hot start, see text for details) and ^c(warm start target, impactor surface temperature set to 1000 K). M_v/M_d is the fraction of the disk in vapor; M_D/M_L ($a > a_R$) and M_{Fe}/M_D ($a > a_R$) are the mass in lunar masses and the iron mass fraction for disk material with equivalent circular orbits exterior to the Roche limit. Other quantities are defined in the text.

Compared to the successful impacts identified in Canup and Asphaug (2001), those found here involve slightly larger impactors ($0.11 \leq \gamma \leq 0.15$ here vs. $0.10 \leq \gamma \leq 0.12$ in CA01), and produce systems with similar amounts of orbiting mass, and somewhat higher amounts of iron and final angular momenta (see Fig. 11 and Section 5.4).

5. General trends in impact outcome

Results from simulations with varied impact parameter ($b' = 0.45$ to 0.85), γ (0.11 , 0.13 , and 0.15), v_{imp} (1.0 to $1.1v_{\text{esc}}$), N ($20,000$ to $120,000$ particles) and initial object thermal state (“warm” vs. “hot”) are shown in Figs. 8 through 11 which contain results from 98 simulations. In general, there are fairly consistent trends in the mass and angular momentum placed into orbit similar to those identified in Canup et al. (2001) and CA01, with both quantities generally increasing with increasing impact parameter. The fraction of iron in the disk, as well as the fraction of the disk originating from the impactor, also both tend to increase with increasingly grazing impacts. Of all of these quantities, the orbiting angular momentum shows the most consistency, while the iron fraction generally has the widest scatter across different simulations, likely a result of the relatively fewer number of SPH particles describing the disk iron.

The maximum yield (both in terms of mass and angular momentum) of iron-depleted material occurs consistently in the impact parameter range of $0.7 < b' < 0.75$. Many of the cases in this “peak” have a similar morphology to that seen in Figs. 2 and 7, with the post-impact impactor re-coalescing into two distinct clumps, the inner of which contains the impactor core and re-collides with the Earth, while the outer contains primarily impactor mantle and avoids direct impact with the Earth, providing the major source of mass for the orbiting disk. For smaller impact parameters, increasingly head-on collisions yield less orbiting material because a smaller portion of the impactor shears past the target during the initial impact. For somewhat larger impact parameters, the impactor typically re-accumulates after the initial impact into a fairly coherent single object, which then re-impacts with a slightly reduced impact parameter due to energy loss associated with the initial impact. For very oblique impacts ($b' > 0.8$) the yields of orbiting material can be large, but they usually contain too much iron to be lunar forming candidates. In general, the mass fraction of orbiting iron increases with impact parameter, as has been found previously (Canup et al., 2001; CA01).

5.1. Effect of resolution and initial thermal state

Figure 8 shows results from simulations in which N and the initial thermal state of the colliding objects were varied for impacts that all had $\gamma = 0.13$ and $v_{\text{imp}} = v_{\text{esc}}$. The scatter in the results shows no clear dependence on either resolution or initial thermal state for the values considered here.

We note that for a 3D simulation, linear resolution scales as $N^{1/3}$, so that characteristic smoothing lengths vary by only about a factor of 1.6 across this span of resolutions (see also discussion in Section 6).

5.2. Effect of impact velocity

Previous high-resolution simulations (Cameron, 1997, 2000, 2001; CA01) considered the limiting case of $v_{\text{imp}} = v_{\text{esc}}$, but higher values would result if the impactor and protoearth had a sufficiently large relative velocity at infinity, v_{∞} . Limits on v_{∞} -values appropriate for a lunar-forming impact provide constraints on the pre-collision impactor and target orbits.

Figure 9 shows the same quantities as in Fig. 8 for simulations all involving the same impactor and target thermal state, with varied N , b' , and $(v_{\text{imp}}/v_{\text{esc}})$. Impacts with $(v_{\text{imp}}/v_{\text{esc}}) = 1, 1.02, 1.05,$ and 1.10 (corresponding to $v_{\infty} = 0, 1.9, 3.0,$ and 4.3 km/sec) produce fairly similar trends in outcome as a function of impact parameter, with the $(v_{\text{imp}}/v_{\text{esc}}) = 1.02$ and 1.05 cases producing slightly higher yields of orbiting mass than $(v_{\text{imp}}/v_{\text{esc}}) = 1.00$. However, as the impact velocity is increased to $1.1v_{\text{esc}}$, an increasing amount of escaping material yields lower peak disk masses and angular momenta; in addition, there appears to be a fairly consistent increase in the fraction of disk iron with increasing $(v_{\text{imp}}/v_{\text{esc}})$ for a given impact parameter. Thus we consider $(v_{\text{imp}}/v_{\text{esc}}) = 1.1$ to be an approximate upper limit for a potential lunar-forming impact.

5.3. Varying impactor to total mass ratio

Figure 10 contains results from a smaller series of runs performed with a slightly higher gamma value ($\gamma = 0.15$) and a reduced total colliding mass of $M_T = 0.95M_{\oplus}$. Similar general trends result. Figures 11a–11b show results of simulations that all involved $v_{\text{imp}} = v_{\text{esc}}$ and the same initial thermal state, but with $\gamma = 0.11, 0.13,$ and 0.15 . Here the orbiting mass is scaled by the total colliding mass. As γ increases, the fractional yield of orbiting material increases for a given impact parameter, as was also found in CA01. Across this range of γ values, the maximum mass and angular momentum yield of iron-depleted orbiting material, which occurs in the $0.7 < b' < 0.75$ range, scales approximately linearly with γ , with

$$\left. \frac{M_D}{M_T} \right|_{\text{MAX}} \approx 0.015 \left(\frac{\gamma}{0.1} \right) \quad (6)$$

for the $v_{\text{imp}} = v_{\text{esc}}$ cases. We note that (6) is also consistent with the maximum yield of iron-depleted orbiting material seen in Cameron’s simulations with $\gamma = 0.3$, where $(M_D/M_T)|_{\text{MAX}} \sim 0.045$ (Canup et al., 2001, their Fig. 2a), as well as that of simulations with $0.12 \leq \gamma \leq 0.2$ reported in Cameron and Benz (1991). Equation (6) thus applies generally across the $0.1 \leq \gamma \leq 0.3$ range for low-velocity impacts involving terrestrial composition objects modeled

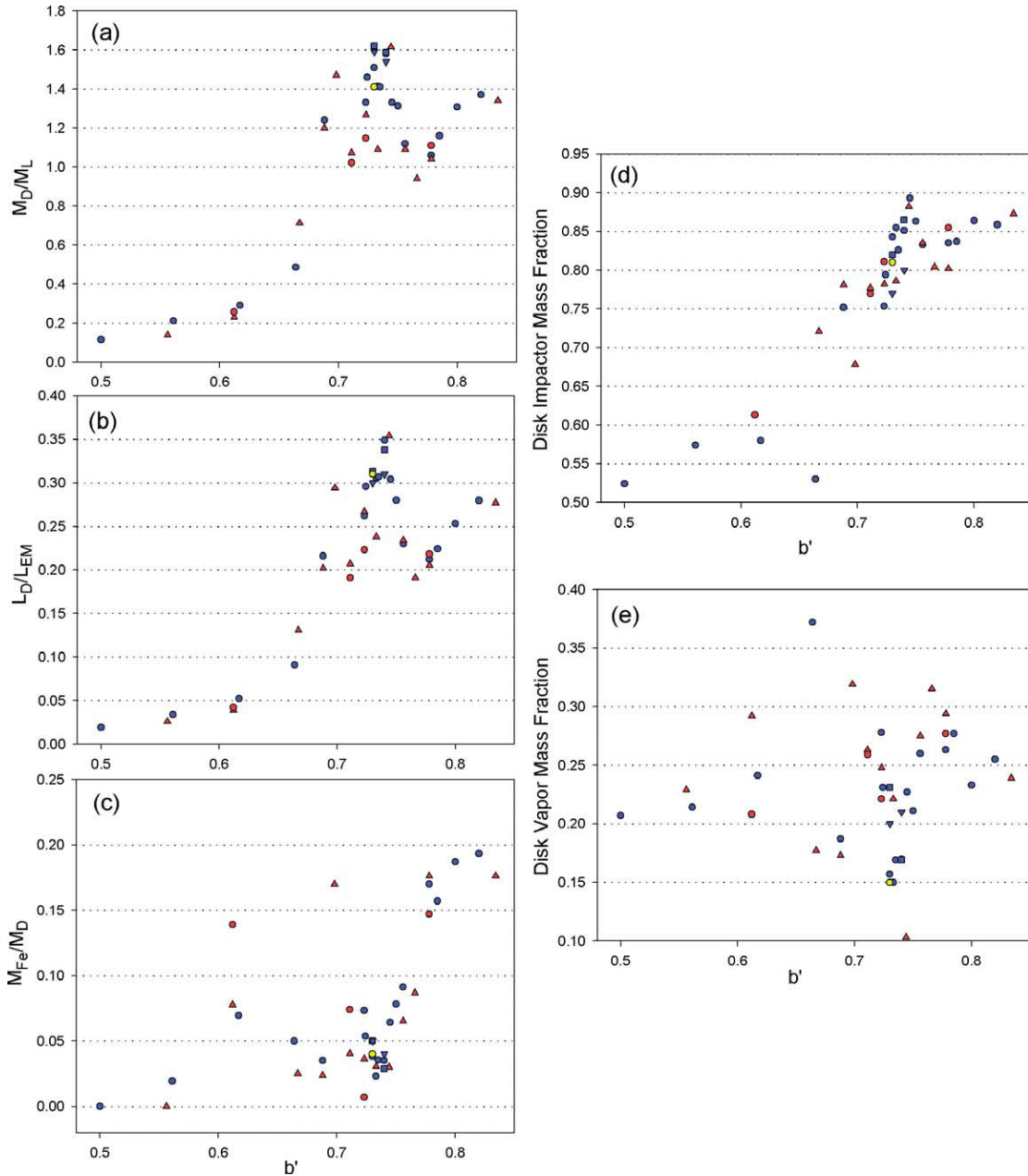


Fig. 8. Results from 40 impact simulations that all had $M_T = 1.02M_\oplus$, $\gamma = 0.13$, and $v_{\text{imp}} = v_{\text{esc}}$, but with varied resolutions and pre-impact thermal states for the colliding objects. Blue symbols are results of simulations utilizing “warm start” objects with surface temperatures set to 2000 K, red are “hot start” objects that were collisionally generated, and yellow is a “warm start” target but an impactor with a surface temperature of 1000 K (see Section 3.2 for details). Triangles, circles, squares, and inverted triangles correspond to resolutions of $N = 20,000, 30,000, 60,000,$ and $120,000$, respectively. (a) Mass of the orbiting disk in lunar masses as a function of scaled impact parameter (with $b' = 1$ corresponding to a grazing impact); (b) angular momentum in the orbiting disk in units of the angular momentum of the Earth–Moon system; (c) mass fraction of orbiting iron; (d) fraction of the orbiting disk mass originating from the impactor; and (e) disk vapor mass fraction.

with ANEOS, without a strong dependence on resolution for $3000 \leq N \leq 120,000$, or on the use of old vs. new ANEOS.

5.4. Comparison with late impact simulations using Tillotson EOS (CA01)

Figures 11a–11d compare results of $v_{\text{imp}} = v_{\text{esc}}$ impacts simulated here using the new Melosh ANEOS vs. those of

CA01 using Tillotson. For the same impactor-to-target mass ratio ($\gamma = 0.11$) and impact parameter, the M-ANEOS simulations produce somewhat less massive disks with proportionally more iron. The first has also been found in previous comparisons between simulations using Tillotson vs. the old ANEOS (Benz et al., 1989), and seems to be a result of ANEOS being a more physically realistic EOS that, e.g., accounts for the energy budget of latent heat dur-

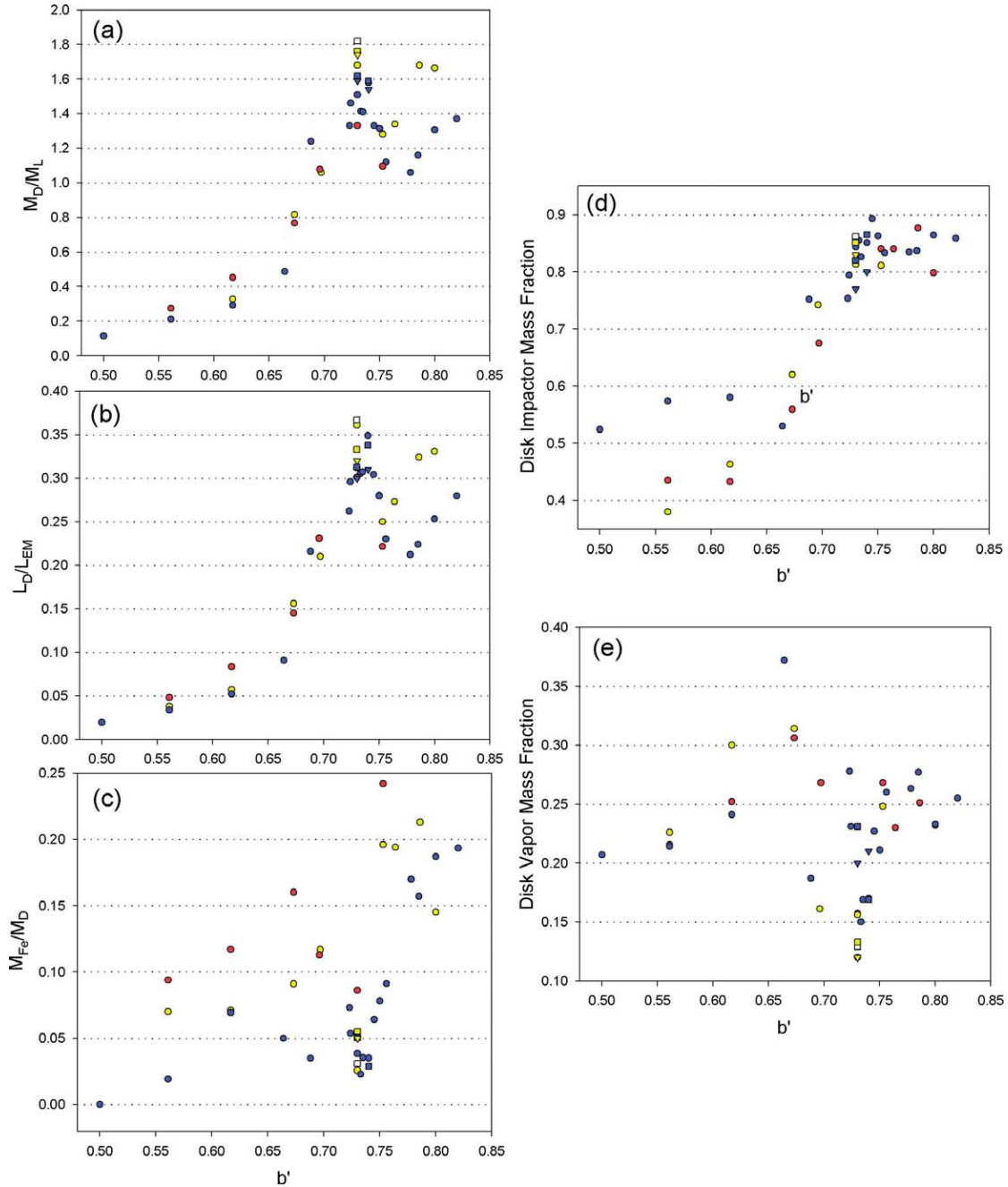


Fig. 9. Results from 40 impact simulations that all had $M_T = 1.02M_\oplus$, $\gamma = 0.13$, and a “warm start” initial thermal state, but with varied resolutions and impact velocities. Blue, white, yellow and red symbols correspond respectively to simulations with $(v_{imp}/v_{esc}) = 1.00, 1.02, 1.05,$ and 1.10 . Shapes vary with simulation resolution as in Fig. 7; frames (a) through (e) plot the same quantities as those in Fig. 7.

ing vaporization.¹³ To obtain the same fractional yield of orbiting mass in an M-ANEOS simulation thus requires a

¹³ Including consideration of latent heat should be most important for impacts whose specific impact energy per unit projectile mass, E_I , is comparable to the heat of vaporization for rock, $E_v \sim 10^{11}$ ergs/g, and less important for impacts with either $E_I \ll E_v$ or $E_I \gg E_v$. For $v_{imp} = v_{esc}$, $E_I = (1 - \gamma)(4\pi\rho/3)^{1/3}GM_T^{2/3}/[\gamma^{1/3} + (1 - \gamma)^{1/3}]$, so that for $\gamma = 0.13$ and $M_T \approx M_\oplus$, $E_I \approx 3.8 \times 10^{11}$ ergs/g, comparable to E_v . Also of a similar magnitude is the specific energy difference between an orbit with

slightly higher impactor-to-total mass ratio (γ -value) than a Tillotson simulation with the same impact parameter and impact velocity, since for a given b' , (M_D/M_T) increases with increasing γ (e.g., Section 4.3). This is why the optimal impactor size range here is $0.11 \leq \gamma \leq 0.15$ vs. $0.1 \leq \gamma \leq 0.12$

$a = 1.5R_\oplus$ and the Earth’s surface, $\sim 10^{11}$ ergs/g. It is thus not surprising that accounting for the latent heat budget results in a somewhat lower yield of orbiting material for simulations using M-ANEOS than those using Tillotson for similar impact conditions.

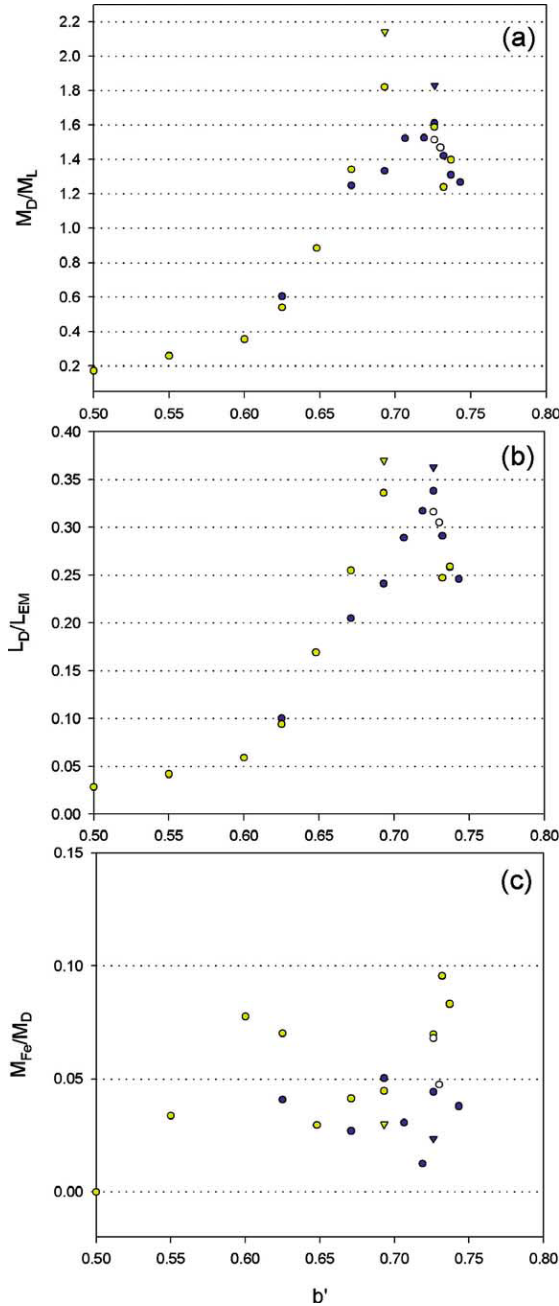


Fig. 10. Results from 23 impact simulations that all had $M_T = 0.95M_\oplus$, $\gamma = 0.15$, and a “warm start” initial thermal state, but with varied resolutions and impact velocities. Blue, white, and yellow symbols correspond respectively to simulations with $(v_{\text{imp}}/v_{\text{esc}}) = 1.00, 1.02, \text{ and } 1.05$; circles and inverted triangles correspond to $N = 30,000$ and $N = 120,000$. (a) Orbiting mass in lunar masses; (b) orbiting angular momentum in units of that of the Earth–Moon system; (c) mass fraction of disk iron.

in CA01. Although the M-ANEOS disks are less massive overall than their Tillotson counterparts, they contain proportionally more material with equivalent orbits exterior to the Roche limit. Thus the characteristic specific angular momenta of the disks in Table 1 (with an average value of $L_D/(M_D\sqrt{GM_\oplus a_R}) \approx 1.13$) are slightly higher than those

of the successful cases in CA01 using Tillotson (average value of $L_D/(M_D\sqrt{GM_\oplus a_R}) \approx 1.07$).

The second difference—that for a given γ and b' value ANEOS produces a more iron-rich disk than a comparable Tillotson run—appears to be primarily due to differences in the mantle materials used with each of the EOS’s. The Tillotson mantle material used in CA01 was basalt, with a reference density of $\rho_o = 2.70 \text{ g/cm}^3$, while here we have used forsterite/dunite with $\rho_o = 3.32 \text{ g/cm}^3$. Thus for an assumed 70–30% rock-iron composition, the ANEOS objects have a relatively thinner mantle and a larger core-to-total radius ratio than the same mass Tillotson object. In addition, the Tillotson targets in CA01 were collisionally generated, which produced initial objects that had a hot, very low density outer layer that was treated as intermediate to a solid and a vapor by the Tillotson EOS; this further accentuated the ANEOS vs. Tillotson radius difference. In all, the radius of a Tillotson protoearth target or impactor from CA01 was about 30% larger than the same mass ANEOS objects considered here.¹⁴ The larger size of the core relative to the mantle for the ANEOS impactors considered here will yield more iron in orbit for the same impact parameter than a Tillotson impactor, since a greater fraction of the iron core can shear past the target with an increasing degree of offset during the initial impact (e.g., Canup et al., 2001).

With both equations of state, the requirements of an appropriately massive and iron-poor disk, together with a planet-disk system with $M_T \sim M_\oplus$ and $L_F \sim L_{EM}$, are best satisfied by impacts with an impact parameter between about 0.7 and 0.75, or for impact angles near 45 degrees. The successful impacts with both EOS’s also share morphological similarities in the impact dynamics (e.g., Fig. 2 here vs. Fig. 1 of CA01). In particular, a common sequence in successful impacts with $\gamma = 0.1$ to 0.15 is:

- (1) the portion of the impactor that shears past the target after the initial impact stretches into an elongated arm-like structure,
- (2) the radially inner portions of the “arm” rotate somewhat ahead of the radially outer portions, providing an opportunity for angular momentum exchange,
- (3) the inner portions of the impactor arm (which contain the impactor’s core) re-coalesce into a quasi-coherent object that then re-impacts the planet, and
- (4) the outer portions clump and are eventually sheared out into a disk during close approaches to the planet, but generally avoid direct secondary re-impacts.

¹⁴ This difference in effective object densities between the M-ANEOS runs here and the CA01 Tillotson runs requires an adjustment in the calculation of b' to allow for direct comparison of the two sets of simulations. For a given impact angular momentum L , $b' = L/L_{\text{graz}}$, and from (5) $L_{\text{graz}} \propto \rho^{-1/6} \propto R^{-1/2}$. Figure 11 shows CA01 results replotted including an appropriate adjustment factor in b' to account for $(R_{\text{Tillot}}/R_{\text{ANEOS}}) \sim 1.3$.

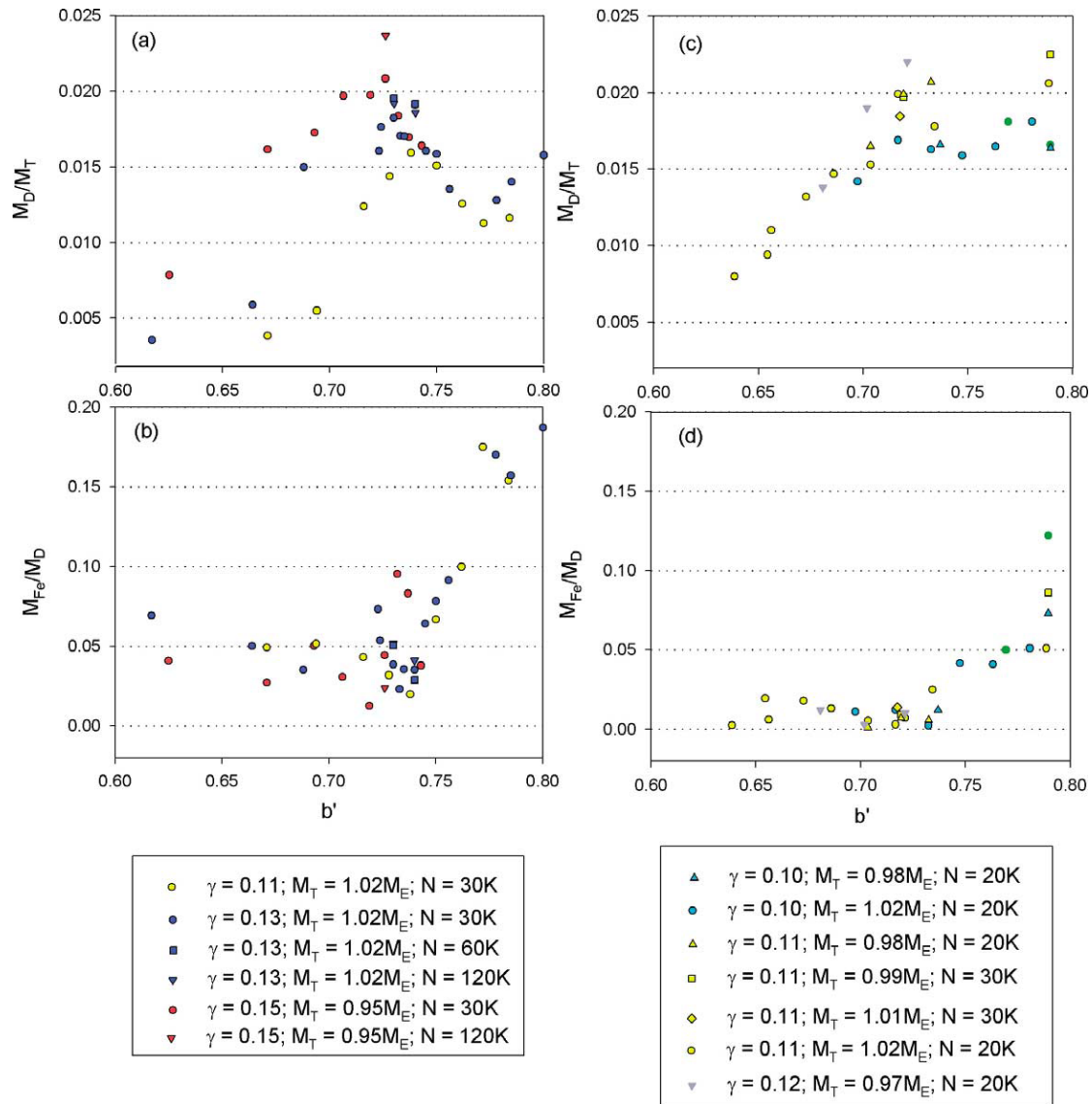


Fig. 11. Results from impact simulations performed here using the new ANEOS (Melosh, 2000) vs. those using the Tillotson equation of state (Canup and Asphaug, 2001). All simulations had $v_{\text{imp}} = v_{\text{esc}}$, but involved varied total masses, resolutions, and impactor-to-total mass ratios (γ). (a) The fraction of the total colliding mass, M_T , that is placed into orbit vs. b' for ANEOS “warm start” simulations; (b) the disk iron fraction for the ANEOS runs; (c)–(d) the same quantities are plotted as in (a)–(b), only here for some of the Tillotson simulations of Canup and Asphaug (2001). Cyan, yellow, gray, blue, and red symbols, correspond to $\gamma = 0.10, 0.11, 0.12, 0.13$, and 0.15 , respectively; shapes vary with both resolution and total colliding mass as shown in the legend boxes.

This sequence is similar to that described by Benz et al. (1987) for three $N = 3000$ particle simulations with $\gamma = 0.1$ to 0.15 (their Section 5.1.3).

5.5. Comparison with results of Cameron (2000, 2001)

A striking difference in the character of the results here vs. those in Cameron (2000, 2001) that utilized the standard ANEOS is the apparent degree of vaporization. From visual inspection, it appears that little of the material in Cameron’s “early-Earth” impact cases (e.g., his runs AS04, AS05, and AS06 in Cameron (2000)) was significantly vaporized, as the material appears to behave like a molten fluid rather than a

partially pressure-supported gas during the simulation. This is particularly apparent when comparing the vertical profiles of the final disk in our Fig. 2, vs. Plates 4, 6, and 8 in Cameron (2000), with the disks here more vertically extended. Increased vaporization would be expected from both the larger total mass and thus impact energy considered here, and the use of the new Melosh ANEOS. Similarly, the early-Earth impacts (Cameron, 2000, his Figs. 7 and 8) find lower final disk (2000 to 4000 K in the 1.5 to $6R_{\oplus}$ range) and protoearth temperatures ($< 10,000$ K) than those in Fig. 6. Our final protoearth is also significantly less oblate than that of Cameron (2000), since the resulting rotational day for the late impact cases is about twice as long as for the early-Earth impacts.

Our impacts are tracked for 22 to 30 hours of simulated time, while those in Cameron (2001) are followed for more than 10 days. Per Eq. (3) and Fig. 5b, for current disk resolutions of $\sim O(10^3)$ particles, simulations longer than about a day may be subject to numerically induced disk spreading. The next generation of simulations and/or disk models will better address this issue. However, regardless of the time scale of disk evolution and lunar accretion, a basic conservation of mass and angular momentum such as is expressed in Eq. (1) will likely be appropriate. We can estimate the satellite masses predicted from Eq. (1) for Cameron’s high-resolution simulations at a simulated time similar to that considered here, and compare them to the final clump/moon masses predicted from his 260-hour simulations. The disk masses and angular momenta for his simulations are given in Canup et al. (2001); again assuming $(M_{\text{esc}}/M_D) = 0.05$, the predicted satellite masses for Cameron’s AS04, AS05, and AS06 runs are 0.723, 0.635, and 0.97 lunar masses, respectively. These predicted masses are similar to the final largest clumps he reports (0.68, 0.73, and 1.09 lunar masses, respectively in AS04, AS05, and AS06).

5.6. Identification of impacts intermediate to the “early-Earth” vs. “late impact” cases

We have shown here that for low-velocity impacts with $0.1 < \gamma < 0.15$, the impact parameter is the most critical quantity for determining orbital yield. The impact parameter range we find to be optimal, $0.7 < b' < 0.75$, is the same¹⁵ as that of the preferred “early-Earth” impacts of Cameron (2000), even though the latter involve a proportionally much larger impactor with $\gamma = 0.3$. Thus this range of impact parameter/angle is the common feature of impacts that produce massive, iron-depleted disks. The implication is that impact geometry plays a key role in orbital mass injection.

Given this range of b' and a desired impact angular momentum, the combination of (γ, M_T) necessary for producing an appropriate protolunar disk can then be analytically estimated for a given $(v_{\text{imp}}/v_{\text{esc}})$. Figure 12 is a plot of M_T vs. γ showing the phase-space of impacts having $L = 1.25L_{\text{EM}}$, $0.70 \leq b' \leq 0.75$ and $1.00 \leq (v_{\text{imp}}/v_{\text{esc}}) \leq 1.10$. Between the two curves is a region of impacts that should all be ideal candidates for producing massive and iron-depleted disks with an impact angular momentum close to that of the Earth–Moon system.

On the upper left, with $M_T \sim M_{\oplus}$ and $0.11 < \gamma \leq 0.15$, is the late impact scenario we advocate here (“late”); on the lower right, with $M_T \sim 0.65M_{\oplus}$ and $\gamma = 0.3$ is the early-Earth impact scenario of Cameron (2000, 2001; “early”). Intermediate to these two cases is a continuous array of impacts that could all likely produce a \sim lunar mass, iron-depleted satellite. The late impact case is distinguished as the

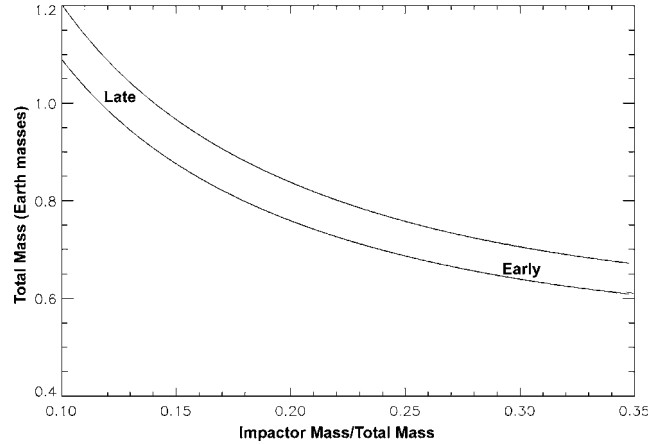


Fig. 12. M_T vs. γ contours for impacts having $L = 1.25L_{\text{EM}}$, $0.70 \leq b' \leq 0.75$, and $1.00 \leq (v_{\text{imp}}/v_{\text{esc}}) \leq 1.10$. Giant impacts with parameters falling between the two curves are predicted to all be good candidates for producing a lunar-mass, iron depleted protosatellite disk. The general regions corresponding to the “late impact” favored here and the “early-Earth” impact scenario of Cameron (2000, 2001) are indicated.

only one in this array of potential impacts that also produces a planet-satellite system with the correct total mass. As one considers impacts that move progressively downward and to the right along these curves, the fraction of the Earth’s mass that must be accreted after lunar formation increases, and with it, the difficulties in maintaining a compositional identity for the Moon distinct from that of the Earth.

6. Conclusion and discussion

The simplest explanation for the Moon’s unusual compositional characteristics is that it is the result of an impact that occurred near the very end of terrestrial accretion. We have thus focused on the “late impact” scenario of Canup and Asphaug (2001), in which the Moon-forming impact occurs when the Earth was $> 95\%$ accreted. We have used SPH to model potential lunar-forming impacts with high resolutions, and our simulations incorporate a new version of the equation of state, ANEOS, “M-ANEOS,” which has been recently revised to include a treatment of the formation of molecular vapor (Melosh, 2000). Thus we expect that the simulations here provide the best representation of vapor production during giant impacts of any SPH simulations published to date.

Results from simulations of the most promising lunar-forming candidates are given in Table 1. The successful impacts—defined as those that produce a sufficiently massive and iron-depleted disk together with a planet-disk system angular momentum $\leq 1.2L_{\text{EM}}$ —involve impactors that contain between 0.11 and 0.14 Earth masses, have a relative velocity at infinity between 0 and 4 km/sec, and an impact parameter between 0.67 and 0.76 (or an impact angle ξ between 42 and 50 degrees, where 0 degrees is a head-on impact). For an isotropic flux of impactors, the probability

¹⁵ The $N = 100,000$ particle simulations of Cameron (2000)—AS04, AS05, and AS06—have $b' = (L/L_{\text{graz}}) = 0.698, 0.730, \text{ and } 0.761$, respectively (from Table 1 in Canup et al., 2001).

of an impact with angle ξ to $(\xi + d\xi)$ is $dP = 2 \sin \xi \cos \xi$ (e.g., Pierazzo and Melosh, 2000); the probability of an impact having $0.67 \leq b' \leq 0.76$ is then $\sim 13\%$.

Maximum circumplanetary disk masses range from 1.5 to 2.1 lunar masses, and disk angular momenta from 0.3 to $0.37L_{EM}$. The disk vapor fraction ranges from 10 to 30%, and the fraction of the disk mass originating from the impactor is greater than 70% for all of the successful lunar forming candidates. For the most successful impacts, we identify the specific source region of the impactor that supplies the majority of the orbiting material: a portion of the leading face of the impactor that was just radially exterior to the primary impact interface. This material is typically heated the least during the impact of any of the impactor material. Adjacent to this region is material that is highly heated and expands rapidly from the front side of the impact site; this material is generally predicted to escape the Earth–Moon system. These findings suggest that the most important physical processes to orbital mass injection are impact geometry and gravitational torques. A simple expression has been identified that approximates the maximum amount of iron-depleted material placed into orbit as a function of the relative size of the impactor vs. target (Eq. (6)); this expression is generally consistent with results produced with both the old and new ANEOS (Cameron and Benz, 1991; Cameron, 2000, 2001; this work) over a wide range in resolution ($N = 3000$ to 120,000 particles).

We have not identified any impacts that produce the massive (e.g., 3–4 lunar masses), centrally condensed disks that would be consistent with the Moon forming entirely from material initially within Roche limit. We instead typically find the majority of the disk material has equivalent circular orbits exterior to the Roche limit. Indeed, some of the disks produced here have higher specific angular momenta than those studied by previous lunar accretion simulations (Ida et al., 1997; Kokubo et al., 2000; Takeda and Ida, 2001). In addition, the majority of the orbiting material is predicted to be in a melt-vapor two-phase state, rather than in solids, as assumed by such models.

The overall predictions for the bulk dynamical quantities of the protolunar disk—i.e., the mass and angular momentum placed into orbit for a given impact—appear relatively insensitive to a variety of initial conditions, including numerical resolution for $10^4 < N < 10^5$, equation of state, and the initial thermal state of the colliding objects. Comparisons with the orbiting mass predictions from even the earliest, lowest resolution simulations with $N = 3000$ (e.g., Benz et al., 1987; Cameron and Benz, 1991) are not vastly different than those obtained here for similar impacts. A limitation of these early works that was perhaps as important as resolution itself was the computational demands of SPH simulations at that time, which greatly limited their number. Increased computational speeds and greater numbers of simulations have since led to the recognition of the dominant impact scaling trends—and the associated predictions

for optimal impact characteristics for producing the Earth–Moon system (Canup et al., 2001; CA01; this work).

Of the dynamical quantities, the mass fraction of orbiting iron is the most variable across the various works; this is not too surprising given that it was essentially unresolved by the earliest simulations, and here is described by a maximum of only $\sim 10^2$ particles. Future generations of higher resolution simulations will better address this issue, and will also allow for longer simulations of the orbiting material, since the latter is affected by the numerical viscosity associated with the disk particle smoothing lengths (Eq. (2)). In addition, to date nearly all of the works modeling giant impacts have utilized SPH; only a limited number of preliminary studies (e.g., Melosh and Kipp, 1989; Melosh and Spitale, 1999) have utilized other hydrodynamic methods (e.g., CTH, a grid based Eulerian code) to model the earliest stages of the impact. Thus the potential influence of SPH-specific traits on simulation outcome remains uncertain, and comparisons with complimentary methods would be desirable.

But in general, results found here and elsewhere imply that low-velocity impacts ($v_{imp} < 1.2v_{esc}$) between similarly sized objects ($0.1 \leq \gamma \leq 0.3$) produce orbiting disks once the impact parameter exceeds about $b'/0.5$. Models of late stage planet accretion (e.g., Agnor et al., 1999) predict that such large, low-velocity impacts should be common, and for an isotropic impactor flux, $b' \geq 0.5$ occurs for 75% of impacts. This suggests that short-lived circumplanetary disks of various mass and composition (and their resulting impact-generated satellites) may be ubiquitous features of collisional planetary systems.

Acknowledgments

A special thanks is due to Jay Melosh and Betty Pierazzo, who generously provided the new M-ANEOS and associated material parameter constants used in this work, as well as valuable advice during its somewhat laborious incorporation into the code. I thank Erik Asphaug and Shigeru Ida for their very helpful and detailed reviews. This work has benefited from many conversations and prior work with William Ward, Richard Mihran, and Erik Asphaug, and from Peter Tambyln's assistance in development of some of the analysis software. SwRI special allocation capital equipment funds are acknowledged for purchase of the computer cluster used for most of the simulations presented here, and Dirk Terrell and Peter Tambyln for their impeccable computer support at the Department of Space Studies. Finally, I am grateful to A.G.W. Cameron for our many correspondences/discussions on this topic, and for his inspiring my interest in these simulations. This work has been supported by the NASA Origins of Solar Systems program.

Appendix A

Here the evolution of the SPH code through a single time step is briefly described, including specific parameter

choices utilized in these simulations. Each i th particle begins the time step with its center position (\mathbf{r}_i), velocity (\mathbf{v}_i), specific internal energy (u_i), smoothing length (h_i), and mass (m_i). The kernel function, $W(r_i, h_i)$, is a spherically symmetric beta spline, which at distance \mathbf{r} from the center of the particle is given by:

$$W(|\mathbf{r}|, h) = \frac{1}{\pi h^3} \begin{cases} 1 - \frac{3}{2}q^2 + \frac{3}{4}q^3, & 0 \leq q \leq 1, \\ \frac{1}{4}(2 - q)^3, & 1 \leq q \leq 2, \\ 0, & q > 2, \end{cases} \quad (\text{A.1})$$

where $q \equiv |\mathbf{r}|/h$ and $\int W(\mathbf{r}, h) d\mathbf{r} = 1$, so that W is akin to a probability density function. The beta spline is centrally-peaked, similar to a Gaussian, but with a zero value for distances greater than $2h_i$ from the particle center. For each particle, the number of overlapping “neighbor” particles is identified for which $|\mathbf{r}_i - \mathbf{r}_j| < 2\langle h_{ij} \rangle$ where the average smoothing length is $\langle h_{ij} \rangle = (h_i + h_j)/2$. The density ρ_i at the center of each particle is then computed by adding contributions from all N neighbors (including the i th particle itself):

$$\rho_i = \sum_{j=1}^N m_j W(|\mathbf{r}_i - \mathbf{r}_j|, h_{ij}). \quad (\text{A.2})$$

Thus the density of each particle is “smoothed” by the contributions of its neighbors (see also Section 3.2). The equation of state is called to compute pressure (P_i) from ρ_i and u_i . ANEOS takes as its inputs ρ_i and T_i (see, e.g., Benz et al., 1989), and so an initial iteration is first required to determine a temperature T_i consistent with ρ_i and u_i . This is accomplished by use of a Newton–Raphson method in combination with a bisection step whenever the prediction would take the solution out of bounds, with the bounds determined by the more restrictive of either fixed physical limits (e.g., minimum temperature of 50 K and maximum temperature of 10^6 K) or those set by results of previous iterations (e.g., if a trial temperature returns a specific internal energy that is too low, then this trial value becomes the new minimum temperature bound). We directly use the ANEOS subroutines rather than a look-up table.

Next the accelerations due to pressure, artificial viscosity, and gravity are computed via momentum conservation, i.e.:

$$\frac{dv_i}{dt} = - \sum_{j=1}^N m_j \left(\frac{P_i}{\rho_i^2} + \frac{P_j}{\rho_j^2} + \Pi_{ij} \right) \nabla_i W(|\mathbf{r}_i - \mathbf{r}_j|, h_{ij}) - G \sum_{j=1}^{N_{\text{Tot}}} \frac{M(|\mathbf{r}_i - \mathbf{r}_j|)}{|\mathbf{r}_i - \mathbf{r}_j|^2} \frac{(\mathbf{r}_i - \mathbf{r}_j)}{|\mathbf{r}_i - \mathbf{r}_j|}, \quad (\text{A.3})$$

where Π_{ij} is artificial viscosity, the first parentheses includes the pressure term and the loss of kinetic energy due to viscous dissipation, and the second term on the right-hand side is the gravitational acceleration, where M is computed via Poisson’s equation for neighbor particles and reduces to the particle mass for distant particles. A hierarchical tree is utilized for the gravitational force calculation (e.g., Hernquist

and Katz, 1989), in which multipole expansions are used to approximate the potential of groups of distant particles, providing an $N \log N$ scaling.

A standard prescription for artificial viscosity is used to mimic shock dissipation, including terms that are linear and quadratic in the velocity divergence of colliding particles (e.g., Balsara, 1995), with $\bar{\alpha} = 1.5$ and $\beta = 2\bar{\alpha}$. The artificial viscosity is operative only for converging particles. The rate of change in h based on (dv_i/dt) values computed in (A.3), together with a requirement that a minimum of 40 and a maximum of 100 neighbors for each particle be roughly maintained.

The rate of change in internal energy due to pressure and artificial viscosity is computed from the energy conservation:

$$\frac{du_i}{dt} = \sum_{j=1}^N \frac{P_i}{\rho_i^2} m_j (\mathbf{v}_i - \mathbf{v}_j) \cdot \nabla_i W(|\mathbf{r}_i - \mathbf{r}_j|, h_{ij}) + \sum_{j=1}^N \frac{1}{2} m_j \Pi_{ij} (\mathbf{v}_i - \mathbf{v}_j) \cdot \nabla_i W(|\mathbf{r}_i - \mathbf{r}_j|, h_{ij}), \quad (\text{A.4})$$

where the first term on the right-hand side is the work due to compression heating or expansional cooling, and the second term is heating due to shock dissipation. The latter is operative for particles with some component of their motion in convergence.

The time step is computed by taking the shortest determined for any of the particles, found by comparing each particle’s Courant limit time ($\sim (h_i/c_i)$ where c_i is the sound speed) to the times associated with a significant change in a particle’s position, internal energy, or smoothing length. Typical time steps during a simulation are \sim a few seconds. Finally, the system properties are evolved using a 2nd-order predictor–corrector method, and the simulation advances to the next step.

References

- Agnor, C.B., Canup, R.M., Levison, H.F., 1999. On the character and consequences of large impacts in the late stage of terrestrial planet formation. *Icarus* 142, 219–237.
- Balsara, D., 1995. Von Neumann stability analysis of smooth particle hydrodynamics—suggestions for optimal algorithms. *J. Comput. Phys.* 121, 357–372.
- Benz, W., Slattery, W.L., Cameron, A.G.W., 1986. The origin of the Moon and the single impact hypothesis I. *Icarus* 66, 515–535.
- Benz, W., Slattery, W.L., Cameron, A.G.W., 1987. The origin of the Moon and the single impact hypothesis II. *Icarus* 71, 30–45.
- Benz, W., Cameron, A.G.W., Melosh, H.J., 1989. The origin of the Moon and the single impact hypothesis III. *Icarus* 81, 113–131.
- Cameron, A.G.W., 1997. The origin of the Moon and the single impact hypothesis V. *Icarus* 126, 126–137.
- Cameron, A.G.W., 2000. Higher-resolution simulations of the giant impact. In: Canup, R.M., Righter, K. (Eds.), *Origin of the Earth and Moon*. Univ. of Arizona Press, Tucson, pp. 133–144.
- Cameron, A.G.W., 2001. From interstellar gas to the Earth–Moon system. *Meteorit. Planet. Sci.* 36, 9–22.
- Cameron, A.G.W., Benz, W., 1991. The origin of the Moon and the single impact hypothesis IV. *Icarus* 92, 204–216.

- Cameron, A.G.W., Ward, W.R., 1976. The Origin of the Moon. In: Proc. Lunar Planet. Sci. Conf. 7th, pp. 120–122.
- Canup, R.M., Ward, W.R., 2000. A hybrid fluid/ N -body model for lunar accretion. In: Proc. Lunar Planet. Sci. Conf. 31st, pp. 1916–1917.
- Canup, R.M., Asphaug, E., 2001. Origin of the Moon in a giant impact near the end of the Earth's formation. *Nature* 412, 708–712.
- Canup, R.M., Ward, W.R., Cameron, A.G.W., 2001. A scaling relationship for satellite-forming impacts. *Icarus* 150, 288–296.
- Canup, R.M., Asphaug, E., Pierazzo, E., Melosh, H.J., 2002. Simulations of Moon-forming impacts. In: Proc. Lunar Planet. Sci. Conf. 33rd, pp. 1641–1642.
- de Pater, I., Lissauer, J.J., 2001. Planetary Sciences. Cambridge Univ. Press, Cambridge.
- Halliday, A.N., Lee, D.-C., Jacobsen, S.B., 2000. Tungsten isotopes, the timing of metal-silicate fractionation, and the origin of the Earth and Moon. In: Canup, R.M., Righter, K. (Eds.), Origin of the Earth and Moon. Univ. of Arizona Press, Tucson, pp. 45–62.
- Hartmann, W.K., Davis, D.R., 1975. Satellite-sized planetesimals and lunar origin. *Icarus* 24, 504–515.
- Hernquist, L., Katz, N., 1989. TREESPH—a unification of SPH with the hierarchical tree method. *Astrophys. J. Suppl.* 70, 419–446.
- Hood, L.L., Zuber, M.T., 2000. Recent refinements in geophysical constraints on lunar origin and evolution. In: Canup, R.M., Righter, K. (Eds.), Origin of the Earth and Moon. Univ. of Arizona Press, Tucson, pp. 397–412.
- Ida, S., Canup, R.M., Stewart, G.R., 1997. Lunar accretion from an impact generated disk. *Nature* 389, 353–357.
- Imaeda, Y., Inutsuka, S., 2002. Shear flows in smoothed particle hydrodynamics. *Astrophys. J.* 569, 501–518.
- Jacobsen, S.B., Yin, Q., 2003. Hf-W, accretion of the Earth, core formation and the origin of the Moon. In: Proc. Lunar Planet. Sci. Conf. 34th. Abstract 1913.
- Jones, J.H., Delano, J.W., 1989. A three-component model for the bulk composition of the Moon. *Geochim. Cosmochim. Acta* 53, 513–527.
- Jones, J.H., Palme, H., 2000. Geochemical constraints on the origin of the Earth and Moon. In: Canup, R.M., Righter, K. (Eds.), Origin of the Earth and Moon. Univ. of Arizona Press, Tucson, pp. 197–216.
- Kaula, W.M., Yoder, C.F., 1976. Lunar orbit evolution and tidal heating of the Moon. In: Proc. Lunar Planet. Sci. Conf. 17th, pp. 440–442.
- Kokubo, E., Canup, R.M., Ida, S., 2000. Lunar accretion from an impact-generated disk. In: Canup, R.M., Righter, K. (Eds.), Origin of the Earth and Moon. Univ. of Arizona Press, Tucson, pp. 145–164.
- Kokubo, E., Makino, J., Ida, S., 2000. Evolution of a circumterrestrial disk and formation of a single Moon. *Icarus* 148, 419–436.
- Lucey, P.G., Taylor, G.J., Malaret, E., 1995. Abundance and distribution of iron on the Moon. *Science* 268, 1150–1153.
- Lucy, L.B., 1977. A numerical approach to the testing of the fission hypothesis. *Astron. J.* 82, 1013–1024.
- Melosh, H.J., 2000. A new and improved equation of state for impact computations. In: Proc. Lunar Planet. Sci. Conf. 31st. Abstract 1903.
- Melosh, H.J., Kipp, M.E., 1989. Giant impact theory of the Moon's origin: first 3-D hydrocode results. In: Proc. Lunar Planet. Sci. Conf. 20th, pp. 685–686.
- Melosh, H.J., Pierazzo, E., 1997. Impact vapor plume expansion with realistic geometry and equation of state. In: Proc. Lunar Planet. Sci. Conf. 28th, pp. 935–936.
- Melosh, H.J., Spitale, J.N., 1999. New results on the giant impact model of the Moon's origin. In: Amer. Geophysical Union Fall Meeting, San Francisco.
- Morishima, R., Watanabe, S., 2001. Two types of co-accretion scenarios for the origin of the Moon. *Earth Planet. Space* 53, 213–231.
- Murray, J.R., 1996. SPH simulations of tidally unstable accretion discs in cataclysmic variables. *Mon. Not. R. Astron. Soc.* 279, 402–414.
- Nelson, A.F., Benz, W., Adams, F.C., Arnett, D., 1998. Dynamics of circumstellar disks. *Astrophys. J.* 502, 342–371.
- Pieri, D.C., Dzierwonski, A.M., 1999. Earth as a planet: surface and interior. In: Weissman, P.R., McFadden, L., Johnson, T.V. (Eds.), Encyclopedia of the Solar System. Academic Press, New York, pp. 209–245.
- Pierazzo, E., Melosh, H.J., 2000. Understanding oblique impacts from experiments, observations and modeling. *Ann. Rev. Earth Planet. Sci.* 28, 141–168.
- Righter, K., 2002. Does the Moon have a metallic core? Constraints from giant impact modeling and siderophile elements. *Icarus* 158, 1–13.
- Solomatov, V.S., 2000. Fluid dynamics of a terrestrial magma ocean. In: Canup, R.M., Righter, K. (Eds.), Origin of the Earth and Moon. Univ. of Arizona Press, Tucson, pp. 323–338.
- Stevenson, D.J., 1987. Origin of the Moon—the collision hypothesis. *Ann. Rev. Earth Planet. Sci.*, 271–315.
- Stewart, G.R., 2000. Outstanding questions for the giant impact hypothesis. In: Canup, R.M., Righter, K. (Eds.), Origin of the Earth and Moon. Univ. of Arizona Press, Tucson, pp. 217–223.
- Takeda, T., Ida, S., 2001. Angular momentum transfer in a protolunar disk. *Astrophys. J.* 560, 514–533.
- Tillotson, J.H., 1962. Metallic equations of state for hypervelocity impact, Rep. GA-3216, July 18, Gen At., San Diego, CA.
- Thompson, C., Stevenson, D.J., 1988. Gravitational instability in two-phase disks and the origin of the Moon. *Astrophys. J.* 333, 452–481.
- Thompson, S.L., Lauson, H.S., 1972. Improvements in the Chart-D radiation hydrodynamic code III: revised analytical equation of state, Technical Rep. SC-RR-710714 (Sandia Nat. Labs).
- Touma, J., Wisdom, J., 1998. Resonances in the early evolution of the Earth–Moon system. *Astron. J.* 115, 1653–1663.
- Ward, W.R., 1998. Earth interactions with an impact-generated disk. In: Origin of Earth and Moon Meeting. Lunar and Planetary Institute Press, Houston, p. 52.
- Ward, W.R., Cameron, A.G.W., 1978. Disc evolution within the Roche limit. In: Proc. Lunar Planet. Sci. Conf. 9th, pp. 1205–1207.
- Weidenschilling, S.J., Spaute, D., Davis, D.R., Marzari, F., Ohtsuki, K., 1997. Accretional evolution of a planetesimal swarm. *Icarus* 128, 429–455.
- Wood, J.H., 1986. Moon over Mauna Loa: a review of hypotheses of formation of Earth's Moon. In: Hartmann, W.K., Phillips, R.J., Taylor, G.J. (Eds.), Origin of the Moon. Lunar and Planetary Institute Press, Houston, pp. 17–56.
- Vickery, A.M., Melosh, H.J., 1987. Orbital evolution of the vapor jet from a giant impact. In: Proc. Lunar Planet. Sci. Conf. 18th, pp. 1042–1043.
- Yin, Qingzhu, Jacobsen, S.B., Yamashita, K., Blichert-Toft, J., Telouk, P., Albarede, F., 2002. A short timescale for terrestrial planet formation from Hf-W chronometry of meteorites. *Nature* 418, 949–952.